Politecnico di Torino

Corso di Laurea in Ingegneria Biomedica
Anno accademico 2021/2022
Sessione di Laurea luglio 2022

Links between wall shear stress topological skeleton and imaging markers of early atherosclerosis at the carotid artery

Relatori:

Prof. Umberto Morbiducci
Prof. Diego Gallo
Valentina Mazzi, PhD

Candidata:

Floriana Marchese
s272681

Vorrei dedicare questa pagina ai ringraziamenti.

Ringrazio innanzitutto la mia famiglia: il sostegno, l'amore e l'appoggio che mi ha regalato ogni singolo giorno mi hanno permesso di ottenere tutti i traguardi più belli della mia vita, e sono davvero fortunata ad averla sempre al mio fianco: papà, mamma, Sissi, siete la mia roccia.

Ringrazio Andrea, per tutto l'amore e la forza che mi ha dato e mi dà sempre; sapere che ci sei ed esserci per te mi rende felice, e mi fai stare bene ogni istante in cui siamo insieme.

Ringrazio tutti i miei parenti e i miei amici più cari: Anna, Salvatore, Nuccio, Valeria, Mara, Francesca, Alice, Antonia, Virginia, Alessia, Elisa, Dita: voglio dirvi grazie perché ho il privilegio di volervi bene e di essere voluta bene da voi.

Devo un fondamentale grazie anche alla dottoressa Valentina Mazzi, che mi ha pazientemente guidato in questo percorso di tesi e che mi ha aiutato in ogni passo di questo lavoro; infine ringrazio il Prof. Morbiducci e il prof. Gallo, per avermi trasmesso la voglia di approfondire lo studio delle tematiche di questa tesi attraverso la passione e il rigore con cui spiegano.

Index

Abstract

Cardiovascular diseases are still the leading cause of death globally. Atherosclerosis, one of the most diffused, consists in the formation of plaques between intima and media layers of the vessel wall. Since this disease develops silently until the vessel lumen is severely narrowed, it is capitally important predicting its onset, which depends on systemic, biological and hemodynamical factors. In particular, haemodynamics and geometry play a localizing role in atherosclerotic lesion formation. In fact, in the arterial tree, atherosclerotic plaques tend to develop at specific sites, characterized by complex geometries and complex blood flow patterns. One of these preferential sites is the carotid artery bifurcation.

For many years, low and oscillatory Wall Shear Stress (WSS) acting on the endothelial cells have been recognized as the main indices of disturbed flow promoting atherosclerosis onset and progression; however, this theory has been recently questioned: new studies highlight how low and oscillatory WSS are significant, but only moderate predictors of plaques localization. In this context, new indicators have been explored: among them, WSS topological skeleton descriptors are receiving increasing interest. The WSS topological skeleton is composed by fixed points and contraction/expansion regions linking fixed points. The interest in WSS topological skeleton analysis arises from its ability to reflect cardiovascular complexity, with direct links to flow features known to be associated with adverse vascular biological events.

The aim of this study is to explore if and how these new topological indicators are linked to the imaging markers of early atherosclerosis at the carotid artery, for the purpose of understanding whether they could be attainable in predicting the onset of this disease.

To do that, 45 ostensibly healthy carotid bifurcation models were considered, on which computational fluid dynamics (CFD) simulations were performed. The variability of the WSS contraction/expansion action along the cardiac cycle and the WSS fixed point residence time were quantified using the WSS topological shear variation index (TSVI) and the WSS Fixed Point Weighted Residence Time ($RT\nabla x_{fp}$), respectively. the analysis has been complemented through the evaluation of the Time Averaged Wall Shear Stress (TAWSS), whose correlation with atherosclerosis is well-established. In particular, areas of the luminal surface exposed to high TSVI (TSVA), high fixed point weighted residence time (wRTA) and low TAWSS (LSA) were computed; different combinations of thresholds and surface of interest have been used.

Bivariate analysis among haemodynamic variables and imaging markers showed significant correlations between WSS topological skeleton descriptors (TSVA, wRTA) and wall thickness in common carotid artery, so as between LSA and contrast enhancement on internal carotid artery.

The results of this study therefore support the association between WSS topological skeleton and markers of vascular disease, making a contribution in understanding the connection between TSVI, $RT\nabla x_{fp}$ and clinical observations.

Chapter 1. Cardiovascular system

1.1 Overall description

The main function of cardiovascular system is letting happen those gas and nutrients exchanges that tissue cells need to survive and to exert their functions.

It consists of heart, blood and a wide network of vessels.

1.1.1 Blood

Blood is a fluid tissue, composed by cellular components – red blood cells, white blood cells and platelets – suspended in a liquid matrix, an aqueous solution called plasma (Blood - Plasma | Britannica). In plasma are also dissolved different substances, capitally important for body's physiology; most of them are organic: glucose, lipids, proteins, glycoproteins, hormones, amino acids and vitamins (An Overview of Blood – Anatomy and Physiology).

1.1.2 Heart

The heart is the organ that pumps blood through the vessels. In fact, contractions of this muscular organ generate the necessary pressure to eject blood into the major vessels, from which it will reach the rest of the body. The internal cavity of the heart is divided into four chambers: two upper ones, called atria, and two lower ones, called ventricles. Systemic circulation is supplied by left side chambers; pulmonary circulation is supplied by the right side chambers (systemic an pulmonary circulation will be explained further ahead).

Unidirectionality of blood flow and absence of backflow are guaranteed by valves, which separate the atrium and the ventricle of each side (bicuspid or mitral valve in the left side, tricuspid valve in the right side) (Structure of the Heart | SEER Training); their opening and closure are regulated by pressure gradients between upper and lower chambers.

1.1.3 Vessels

Blood vessels include arteries, capillaries, and veins.

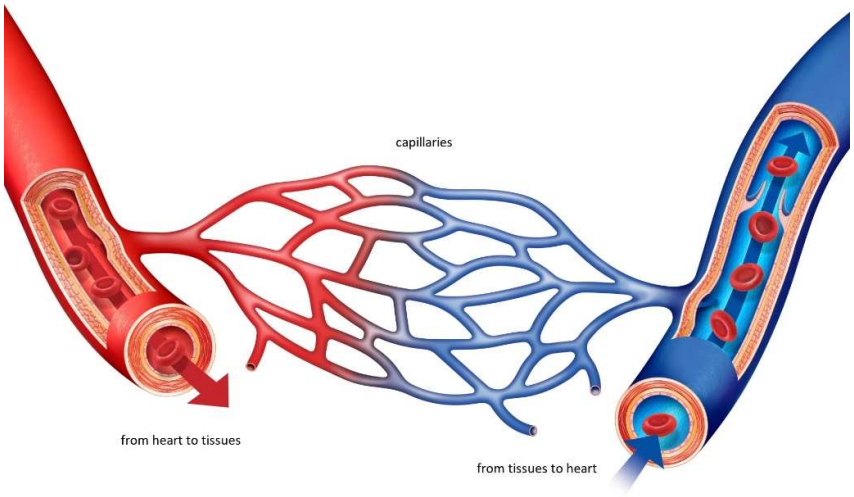

Figure 1. Blood vessels: arteries, capillaries and veins

Arteries carry blood away from the heart to peripheral organs; they branch into smaller vessels (arterioles), that further divide into capillaries: this is where gas, ions, nutrients and wastes are exchanged between blood and tissues cells. Then blood flows into venules (literally “little veins”), which merge to form veins, larger blood vessels that transport blood back to the heart (Figure 1) (Classification & Structure of Blood Vessels | SEER Training).

Cardiovascular system is composed by two subsystems:

- the pulmonary circuit, which allows blood to take up O2 and to get rid of CO2 through gas exchange between blood and inhaled air;
- the systemic one, that is responsible for supplying oxygen and nutrients to tissues and to take away wastes produced by cellular metabolic activity.

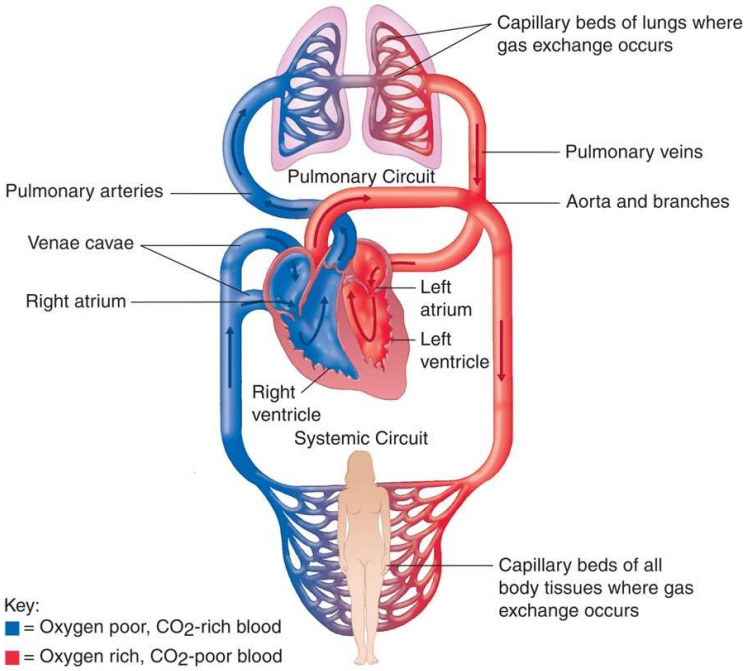

Figure 2. Circulatory system. Pulmonary and systemic circuits.

Oxygen-rich blood is carried from the left ventricle of the heart to body tissues though systemic arteries; after gas and nutrients exchange, systemic veins carry the blood, now poorer in O2, to the right atrium. Then blood reaches the right ventricle, that contracts and pushes it through the pulmonary valve into the pulmonary artery, which takes it to the lungs. In the lungs, the blood cells exchange carbon dioxide for oxygen. The oxygenated blood returns to the heart via the pulmonary veins and enters the left atrium, then it flows through mitral valve into left ventricle, which pumps it into systemic circulation (Figure 2) (17.2D: Systemic and Pulmonary Circulation - Medicine LibreTexts).

1.2 Blood vessels: function and structure of vessels walls

Considering the whole picture of cardiocirculatory system, it can be easily deducted that arteries and veins profoundly differ in function, and this difference reflects in their structure.

In fact, arterial walls need to be thick, strong and elastic, since they have to efficiently propagate the mechanical wave generated by heart contractions, allowing blood to effectively reach every district of the body . On the other hand, veins, which stand a much lower pressure, have thinner walls and larger lumens, so that more blood can easily flow with less vessel resistance. In addition, many veins in our body have valves that prevent the backflow of blood (Figure 3) (Chaudhry et al., 2022; Tucker et al., 2022).

Vessels walls, whether they are arteries or veins, are characterized by a layered structure; from the innermost to the most external one, three layers can be identified (17.2D: Systemic and Pulmonary Circulation - Medicine LibreTexts):

- Intima: it is composed by an inmost single layer of cells, called endothelium, and from a thin subendothelial layer containing collagen fibers (basal lamina).
  Endothelial cells are directly in contact with bloodstream, regulating the exchanges and forming a barrier between the blood and the underlying thrombogenetic tissues; maintaining the integrity of the endothelium is therefore capitally important to preserve vessels functionality. Moreover, endothelial damage can be a concurrent cause in the onset of atherogenesis.
  Basal lamina has an important structural function and a key role as filter in exchanges between vessels and interstitium.
  An internal elastic sheet is interposed between the intimate and the media.

- Media, or muscle layer: it generally constitutes the thickest layer of the wall, and it's composed of an alternation of layers of smooth muscle cells and elastic fibers. It is responsible for the propagation of the heart's systolic impulse, consenting blood to be propelled into the vessels.
  In physiological conditions, smooth muscle cells regulate vasoconstriction and dilation of vessels; if put in contact with blood, the tissues of this layer can be highly thrombogenetic.

- Adventitia: it consists of connective tissue containing fibroblasts, elastic fibers, nerves and the vasa vasorum, small vessels that supply the walls of larger arteries and veins. Vascularization of adventitia is responsible for the oxygen and nutrients supply to the middle tunic, that receive them by diffusion; between media and adventitia there is another elastic layer, called external elastic sheet.

The layered structure of vessel walls gives rise to anisotropic mechanical properties, with different elastic moduli in the axial and circumferential directions (Azuma & Hasegawa, 1973; Camasão & Mantovani, 2021; Zhou & Fung, 1997).

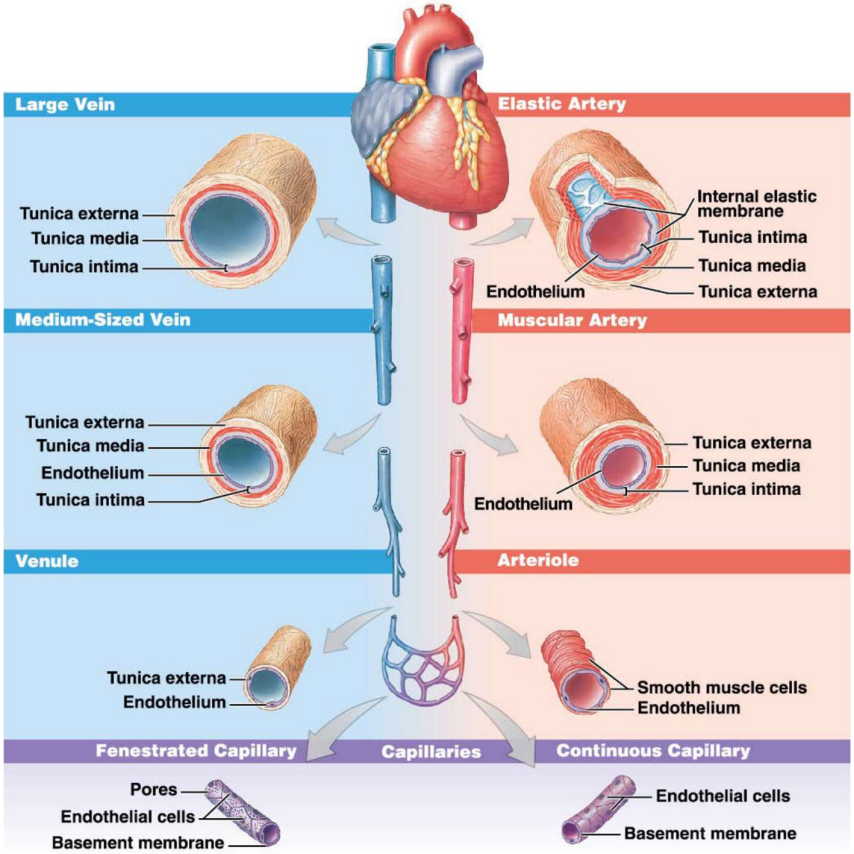

Figure 3. Structure of blood vessels walls

1.3 Cardiovascular diseases

Cardiovascular diseases (CVDs) are nowadays the leading cause of death globally, and their burden in terms of mortality and contribute to disability continues to increase all over the world. (Roth et al., 2020). A great number of CVDs fall into the category of arteriosclerosis, a general name for a group of conditions that cause arteries to become thick and stiff.

The three main types of arteriosclerosis include: arteriolosclerosis, that describes cellular or hyaline thickening of arterioles walls, with consequent loss of their elasticity; Monckeberg medial calcific sclerosis (MMCS), which is the calcification in the internal elastic lamina or in the middle layer of muscular arteries; atherosclerosis (dos Santos et al., 2021), on which this study is focused and that therefore needs a wider dissertation.

1.3.1 Atherosclerosis

Atherosclerosis is a disease characterized by low-grade, chronic inflammation of the arterial walls of large and medium-sized arteries. It consists of an inflammatory cascade that leads to the development of the atheroma, a plaque formed by a necrotic core of lipids (especially cholesterol), from a fibrous outer capsule and a series of different cell types such as macrophages, platelets, fibroblasts . Atheromatous plaques grow between the tunica media and the tunica intima: over time this causes the thickening and stiffening of the vessel walls, and the narrowing of the lumen, so that normal blood flow is hampered (Figure 4) (dos Santos et al., 2021; Lusis, 2000).

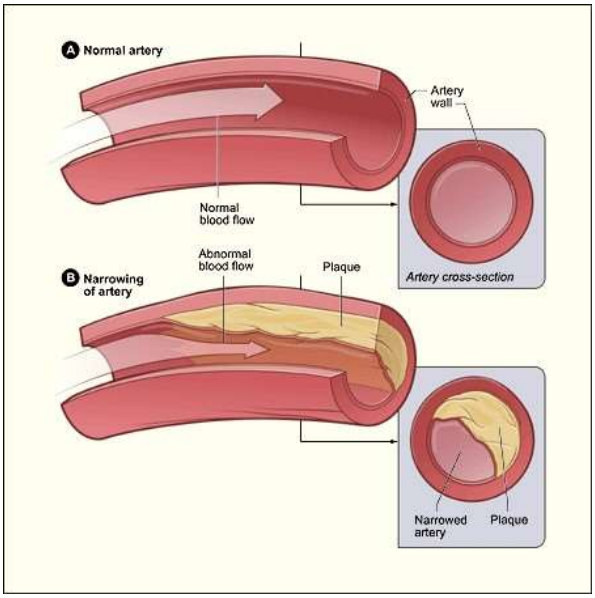

Figure 4. Atherosclerosis: A) Normal artery with a normal blood flow, B) Narrowed artery with abnormal blood flow

Atherosclerosis typically grows slowly and silently for many years, not giving symptoms until the luminal diameter of the vessel has been sensitively decreased, by 70 to 80 percent. Therefore, in westernized societies, it is the underlying cause of about 50% of all deaths (Lusis, 2000).

Consequently atherosclerosis, when it causes the obstruction of the major arteries of our body, can lead to very severe diseases (Arteriosclerosis / Atherosclerosis - Symptoms and Causes - Mayo Clinic):

- coronary heart disease, when the plaque builds-up in the coronaries, impeding oxygen and nutrients to reach the heart; in this situation heart attack or an angina can follow;

- peripheral artery disease, when the plaque blocks an artery delivering blood to the extremities (legs, arms and pelvis), which could get gangrenous;
- chronic kidney disease, when the plaque obstructs renal arteries, causing a loss of kidney function;
- carotid artery disease, when the plaque builds-up in the carotid arteries; in this case, brain cells are deprived of oxygen and a stroke can occur (Figure 5).

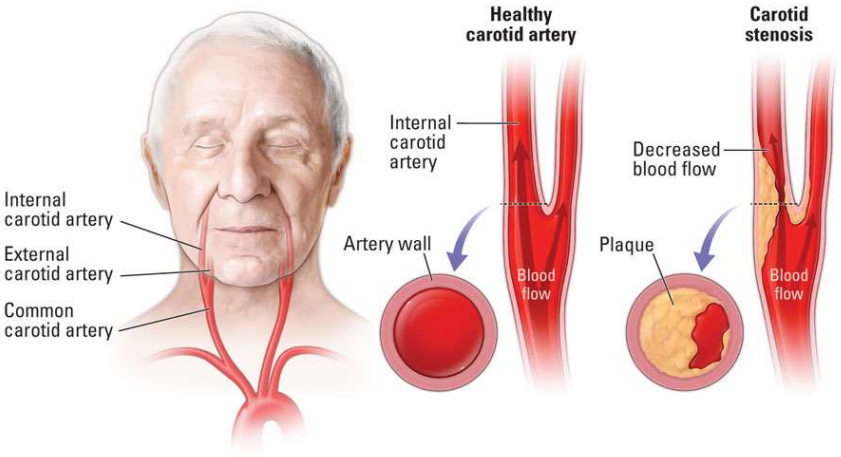

Figure 5. Carotid artery desease

Chapter 2. Hemodynamics

Hemodynamics is the branch of physics that studies flowing blood and all the solid structures through which it flows (Secomb, 2016). This specific field of mechanics, that involve both fluid and solid mechanics, is concerned with the relationship between pressures and flows and their distribution in a network of blood vessels. We are therefore going to briefly examine blood rheological properties of blood, general aspects and laws of flow mechanics and their application in modelling blood flow in vessels, focusing at the end on carotid artery.

2.1 Rheologic properties of blood

The mechanical forces exerted on blood, resulting from blood flow and blood pressure, can be represented using the concept of stress. Stress can be defined as the force per unit area acting on an area ΔS of the surface, and its value at a point can be more rigorously calculated as the limiting value of the force per unit area, as the area ΔS of the surface being considered shrinks to zero around that point. Considering a three-dimensional Euclidean space, the stress tensor has nine components σ_{ij}, where i, j can assume values from 1 to 3; each component represents the traction force in the i^{th} coordinate direction acting on a surface whose normal vector is in the j^{th} coordinate direction. When the values assumed by i and j coincide (i=j), the stress component is referred to as a normal stress, because it acts perpendicularly (normally) to the surface; when they differ (i≠j), the stress component acts parallel to the surface and is referred to as a shear stress

These mechanical forces exerted on blood cause its motion.

Let thus consider a general and simplified case, consisting of a fluid moving between two plates in a bidimensional Cartesian space; the lower plate, placed at y=0, has velocity equal to zero, whereas the upper one, at y=h, moves parallel to itself in the x direction with constant velocity v_x. According to the non-slip boundary condition, the speed of the fluid layer in direct contact with the solid boundary (the platelet in this case) is identical to the velocity of this boundary (Rapp, 2017). This leads to the establishment of velocity gradient, so that the velocity of fluid particles travelling parallel to the wall increases from zero to a maximum value at y=h. The velocity gradient is called shear rate, and it is expressed by Eq. 1:

$$\gamma = \frac{dv_x}{dy} \qquad \text{Eq.1}$$

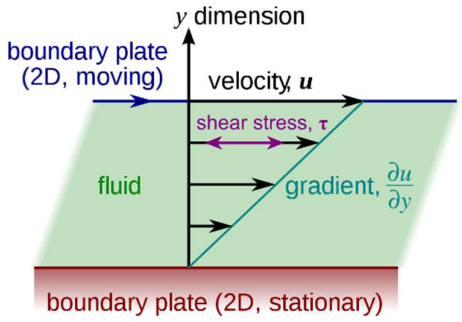

Figure 6. Fluid flowing between two parallel plates

So, shear rate can be defined as the rate at which adjacent layers of fluid move with respect to each other (Papaioannou & Stefanadis, 2005).

The ratio of the shear stress to velocity gradient is called viscosity (μ), which describes the resistance of the fluid to flow; it is the macroscopic expression of the internal friction between the fluid laminas sliding one onto the other.
So, in this simplified and bidimensional configuration – 3D geometries require a more complex definition of shear stress, since stress state is described by a second-order tensor (Gasser, 2021) -, the relationship between shear rate, shear stress and viscosity can be simply expressed by Eq.2:

$$\tau_{xy} = -\mu\dot{\gamma} = -\mu\frac{\partial v_x}{\partial y} \qquad \text{Eq.2}$$

Moreover, this relation is valid only for Newtonian fluids: in this case, viscosity is an intrinsic property at a given temperature and pressure, independent of shear rate. However, blood shows non-Newtonian properties: the relationship between shear stress and shear rate is therefore non-linear (Figure 7) and its viscosity depends on pressure, temperature and shear rate.

Different mathematical models have been developed in order to describe the non-newtonian nature of blood rheological behaviour: the most important ones are Bigham, Casson, Power-Law (plus Generalized Power-Law) and Casson models.

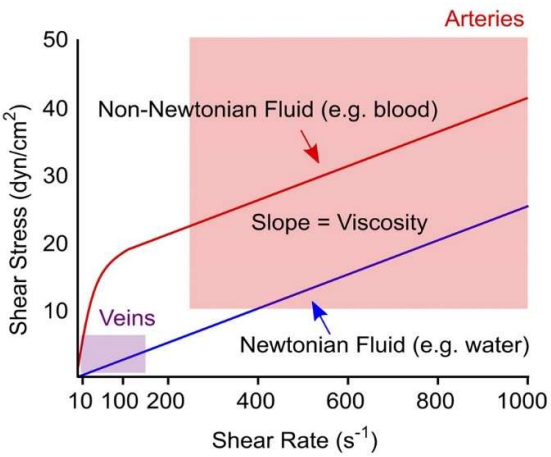

Figure 7: Shear stress-shear rate relationship for Newtonian fluid and blood; the red area represents the shear stress and shear rate ranges typical for arteries, the purple area represents the shear stress and shear rate ranges typical for veins.

Blood viscosity increases at very low shear rates; in figure 7 this is represented by the incrementation of the slope for red line at the left of the diagram. Because of this behaviour, blood can be defined as a shear-thinning fluid.

This phenomenon is due for the most part to red blood cells (RBCs) rheological features (Secomb, 2016). In fact, when velocity of blood and shearing forces acting on the cells are very low, RBCs tend to aggregate into linear arrays called rouleaux, that interact to form three-dimensional structures and create more interference with the flow (Meiselman & Baskurt, 2003; Secomb, 2016).
High values of haematocrit, or the volume fraction of red blood cells, whose value in an adult is usually assumed to be equal to 45%, can promote red blood cells adhesion and leads to high values of blood steady shear viscosity (Sousa et al., 2016).

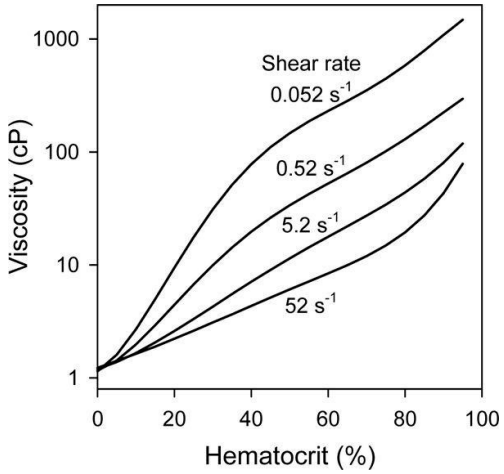

Figure 8. Dependence of the human blood viscosity on haematocrit, for indicated shear rates

The importance of the role of aggregation of RBCs in increasing viscosity can be clearly understood comparing entire blood behaviour with another fluid, consisting of erythrocites in a Ringer solution (Chien, 1970). This solution is characterized by the same viscosity that plasma has, but it does not contain fibrinogen, which is responsible for the aggregation in rouleaux (Figure 9).

The rheological behaviour of erythrocytes conditions blood viscosity not only at low shear rate, but also at high shear rates; in fact, if erythrocytes are hardened, the viscosity results independent of shear rate and higher than the viscosity of normal red blood cells in the same medium (Figure 9). It therefore emerges that at high shear rates the deformability of red blood cells is responsible for the reduction in blood viscosity (Sousa et al., 2016). In fact, in this flow condition, their highly deformability let them assume an ellipsoidal shape, and orienting themselves with the flow streamlines they offer less resistance (Meiselman & Baskurt, 2003).

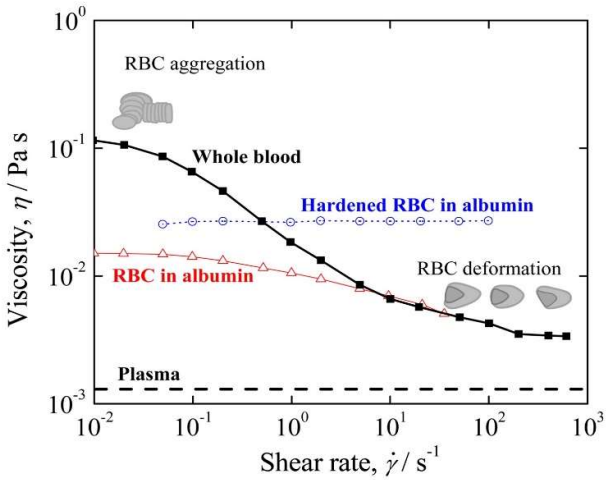

Figure 9. Dependence of the viscosity on the shear rate for three different red blood cells suspensions

Even if blood is a non-newtonian and non-homogeneous fluid, in arteries the values (in the range of hundreds or thousands) of blood flow rates and of diameter (> 0.3 mm) permit to consider it as a Newtonian and homogeneous fluid with valid simplification (Secomb, 2016).

Therefore in large arteries viscosity may be assumed as constant and equal to 3.5 cP (Ayyaswamy, 2016). Viscosity of blood depends on state the temperature and on the state of motion of the fluid, density depends on the temperature and it can be calculated as follows:

$$\rho = (1 - Ht)\rho_p + Ht\rho_{rc} \qquad \text{Eq.3}$$

where Ht is the haematocrit, ρ_p is the plasma density (ρ_p=1035 kg/m^3) and ρ_{rc} is the particles density (ρ_{rc}=1090 kg/m^3). So, the blood density value is 1060 kg/m^3.

2.2 Reynolds number

Considering a fluid with density ρ and viscosity μ, whose flow is characterized by a typical velocity v and typical length L (for a tube L is the diameter), the magnitude of the inertial and viscous terms may then be estimated through a dimensionless parameter called the Reynolds number.
Reynolds number (Re) is a defined as the ratio of the inertial term to the viscous term (Secomb, 2016):

$$\mathrm{Re} = \frac{\rho v L}{\mu} = \frac{v L}{\nu} \qquad \text{Eq.4}$$

ν= kinematic viscosity.

The value assumed by Reynolds number describes the fluid flow condition and the energy content of the flow:

- Re < 2000: the inertial term is negligible, and liquid particles move smoothly in adjacent planes (laminae) parallel to the tube wall: this type of flow is called laminar. This is the least energetic flow condition.
- 4000<Re<10000 the flow is transitional.
- Re>10000: flow becomes irregular and unstable, with fluid moving in swirls and irregular patterns. This type of chaotic flow is called turbulent flow, and it involves unpredictable fluctuations of velocity. This is the most energetic flow condition.

In the normal body, blood flow in vessels is generally laminar; even in arteries, characterized with high shear rate, Reynolds numbers of arterial flow do not go further the critical value (Ayyaswamy, 2016), remaining in the range of hundreds to low thousands. So, in physiological conditions, the blood flow is laminar or at most transitional; however, flow fields can be sensitive to geometrical irregularities, that can be non-physiological in case of pathologic alterations or presence of vascular protheses in the vessel.

2.3 Navier Stokes equations

The mathematical description of local flow phenomena in artery models requires the application of the three-dimensional, time-dependent, incompressible Navier-Stokes equations and of corresponding constitutive relations (Perktold et al., 1999). In order to consider how they can be expressed in this case, we have to start from the momentum and mass balance equations. If $\boldsymbol{v}$ =(v_x,v_y,v_z) is the velocity vector and ρ is the density, then the conservation of mass implies that:

$$\frac{D\rho}{Dt} + \rho(\nabla \cdot \boldsymbol{v}) = \frac{D\rho}{Dt} + \rho\left(\frac{\partial v_x}{\partial x} + \frac{\partial v_y}{\partial y} + \frac{\partial v_z}{\partial z}\right) = 0 \qquad \text{Eq.5}$$

where $\frac{D\rho}{Dt}$ is the material derivative of ρ and is equal to $\frac{\delta\rho}{\delta t} + \boldsymbol{v} \cdot \nabla\rho$.

Conservation of momentum leads instead to:

$$\rho\frac{D\boldsymbol{v}}{Dt} = -\nabla p - \nabla \cdot \boldsymbol{\tau} + \rho\boldsymbol{g} \qquad \text{Eq.6}$$

where $\frac{D\boldsymbol{v}}{Dt}$ is the material derivative of $\boldsymbol{v}$, $\boldsymbol{\tau}$ is the stress tensor, ∇p is the pressure gradient, $\boldsymbol{g}$ is the gravity force.

Continuity equation (Eq. 5) and momentum conservation equation (Eq. 6) are referred to as the Navier-Stokes equations.

These equations can be further modified considering blood as an incompressible Newtonian fluid; in this case its density ρ=ρ(t,x,y,z) can be considered as a constant ($\frac{D\rho}{Dt}$ becomes equal to 0), and so its viscosity μ.

Therefore, Eq.5 becomes:

$$\nabla \cdot \boldsymbol{v} = 0 \qquad \text{Eq.7}$$

where $\nabla\boldsymbol{v}$ is the velocity gradient, and Eq.6 becomes:

$$\rho\frac{D\boldsymbol{v}}{Dt} = \rho\boldsymbol{g} - \nabla p + \mu\,\nabla^2\,\boldsymbol{v} \qquad \text{Eq.8}$$

where $\nabla^2\boldsymbol{v} = \nabla(\nabla \cdot \boldsymbol{v})$ is the Laplacian of $\boldsymbol{v}$.

Solving the Navier-Stokes equations, for a given geometry and a set of boundary conditions, permit to compute fluid velocity and its pressure. However, their complexity let these equations be analytically solved only in a few simple cases; more complex geometries require Navier-Stokes equations to be numerically solved.

2.4 Poiseuille's law

The simplest model to describe blood flowing into vessels consists of a laminar, steady, incompressible, fully developed flow of a Newtonian fluid through a straight, rigid, cylindrical, horizontal tube of constant circular cross-section; this model is called the Hagen-Poiseuille flow (Ayyaswamy, 2016).

In this case, fluid velocity has a parabolic profile (Figure 10), described by the following equation (Eq.9):

$$v(r) = -\frac{\Delta P(R^2 - r^2)}{4\mu L} \qquad \text{Eq.9}$$

where *L* is the length and *R* is the radius of the vessel, μ is the viscosity of the fluid and *ΔP* is the difference of pressure between the two extremities of the tube; *ΔP* gives the driving force to the fluid.

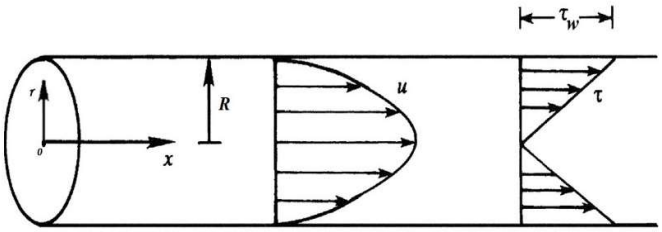

Figure 10. Poiseuille flow: velocity profile and shear stress profile

Velocity value at the wall (*r*=*R*) is equal to zero, whereas at the centre of the tube (*r*=0) the value is maximum and equal to:

$$v_{max} = -\frac{\Delta P\, R^2}{4\mu L} \qquad \text{Eq.10}$$

Average velocity is instead equal to one half of the peak velocity and it is proportional to the volume flow rate *Q*, as shown in Eq.11 :

$$v_{mean} = \frac{Q}{\pi R^2} = -\frac{\Delta P\, R^2}{8\mu L} = \frac{v_{max}}{2} \qquad \text{Eq.11}$$

Volume flow rate Q is calculated integrating the velocity across the circular cross-section of the tube:

$$Q = \int_0^R 2\pi r v(r) dr = \frac{\pi R^4 \Delta P}{8\mu L} \qquad \text{Eq.12}$$

The applicability of Poiseuille's law requires a long list of conditions that circulatory system does not strictly comply with: in fact, blood flow in the circulatory system is generally unsteady and pulsatile, the velocity profile is rarely fully parabolic, arteries are neither straight (radius decreases along the vessel) or rigid, vessels are characterized by branching and curvatures (Secomb, 2016) and blood is not a Newtonian fluid. However, there remain many situations where the Hagen-Poiseuille model is reasonably applicable (Ayyaswamy, 2016) and so it is widely used to obtain operative clinical results.

2.5 Wall Shear Stress

In figure 10 is also shown the shear stress profile of a fluid in the Poiseuille flow conditions, described in the previous chapter: the shear within the flow is zero at r = 0 and it increases linearly with r, reaching a maximum at r = R, the tube radius.

This behaviour can be mathematically defined starting from Eq.13, that expresses the equilibrium of forces acting on the fluid:

$$\tau 2\pi r L = \Delta P \pi r^2 \qquad \text{Eq.13}$$

Therefore, it can be inferred that the shear stress τ is:

$$\tau(r) = \frac{\Delta P r}{2L} \qquad \text{Eq.14}$$

The maximum value, reached at the wall of the pipe, is known as Wall Shear Stress (WSS); in this specific case it is given by:

$$WSS = \frac{\Delta P R}{2L} \qquad \text{Eq.15}$$

Considering WSS applied to circulatory system, blood flow exerts WSS onto the frictional apical surfaces of endothelial cells lining the vessel lumen (Dessalles et al., 2021; Fernandes et al., 2018). In the clinical field, computational fluid dynamics in 3D reconstructions of the arteries allow to assess it, applying patient-specific flow measurements (Wentzel et al., 2012); knowing the mean fluid flow rate Q, fluid viscosity μ, and the physical dimensions of blood vessels (radius R), WSS can be operatively computed using Poiseuille's law (Eq. 16) (Ballermann et al., 1998):

$$WSS = \frac{4Q\mu}{\pi R^3} \qquad \text{Eq.16}$$

The typical values of WSS in arteries and less than 10 dyn/cm2 (1 Pa) in humans, and levels of wall shear stress are significantly lower in the venous circulation (Secomb, 2016).

WSS exerts only on ECs, affecting their activity: it causes cell deformation (strain), which raises cytoskeletal tension (Figure 11), and this influences endothelial permeability, which must remain sufficiently low in order not to let thrombogenic subendothelial matter to enter in contact with blood. Moreover, endothelium responds to shear stress through various pathophysiological chemical patterns, depending on the kind and the magnitude of shear stresses (Papaioannou & Stefanadis, 2005). This point will be further discussed in the following chapter.

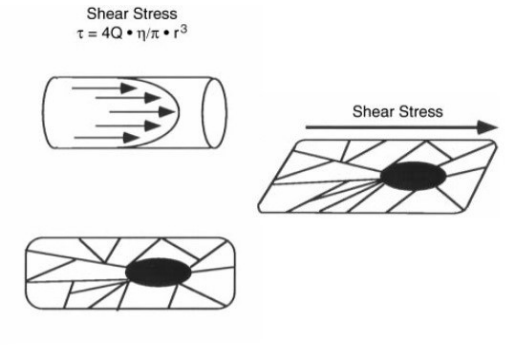

Figure 11. Deformation of ECs due to WSS action

2.6 Hemodynamics role in atherosclerosis

Onset and progression of vascular disease is promoted by systemic, biological and hemodynamic risk factors (Morbiducci et al., 2016).

Even if the association between atherosclerosis and systemic factors (smoking, age, diabetes mellitus, level of HDL,…) is generally well known also in non-scientific world, as part of general knowledge, the role of hemodynamics and vessel geometry is usually less in the public eye, but crucial still. Atherosclerosis

is in fact a focal disease: in the arterial tree, plaques are located at specific sites, characterized by complex geometries and blood flow patterns (Gallo et al., 2015; Wentzel et al., 2012). In this subchapter the interconnection between geometry, flow patterns and pathophysiology will be analysed.

From many studies it emerges that WSS magnitude and type have a pivotal role in the scenario of atherosclerotic risk factors; in particular, low and oscillating WSS promotes the progression of the disease (Chatzizisis et al., 2008; Giddens et al., 1993; Ku et al., 1985; Wasilewski et al., 2013). This behaviour of WSS mainly occurs in sites such as side-branches, the outer waist of bifurcations, or the inner curve of arteries (Wentzel et al., 2012); here there are recirculation and flow separation regions, with WSS values near zero and high shear stress gradient. In fact, geometry has been proven to have a major influence on the blood flow distribution ("geometry shapes the flow") and thus on the hemodynamic indices related to vessel walls (Friedman et al., 1983; Malota et al., 2018; Morbiducci et al., 2016).

By contrast, high unidirectional wall shear stress may exert a protective effect against the induction of atheromatous lesions (Wentzel et al., 2012).

Both low and oscillatory wall shear stress also contribute to an increased fluid residence time (RT) ; this corresponds to a longer contact time of blood-carried particles that are involved in atherogenic inflammatory cascade (i.e. platelets, macrophages, low density lipoproteins) with the artery wall (Kunov et al., 1996). High RTs therefore favour the retention of these agents into arterial wall, phenomenon that is an important mechanism in the atheroma formation (Wasilewski et al., 2013).

Shear stress acting on endothelial cell monolayer play a significant part in their physiological alignment and elongation in the direction of blood flow; so, when marked oscillations in the direction of wall shear stress take place, ECs may change their shape, becoming more polygonal and losing a defined alignment pattern (Figure 12). At the cytoskeletal level, undisturbed flow leads to prominent actin stress fibers that are aligned in the direction of flow, whereas ECs subjected to disturbed flow exhibit shorter and randomly oriented actin filaments (Dessalles et al., 2021).

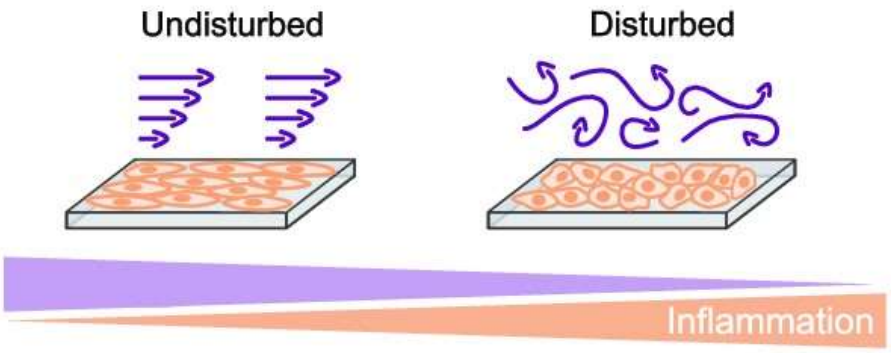

Figure 62. Effect of undisturbed/disturbed flow on endothelial cells.

These morphological changes, in combination with the prolongation of the residence time of circulating particles, can lead to an increase in permeability of the endothelial layer, that allows infiltration of lipids, fibrinogen, fibrin and other atherogenic particles into the intima (Wasilewski et al., 2013).

Moreover, endothelial cells respond to shear stress not only mechanically, but also chemically: in fact, shear stress resulting from blood flow generates biochemical signals that modify signalling pathways, and gene and protein expression. This mechanism, called mechanotransduction is due to the presence in the ECs of numerous mechanoreceptors, transductors capable of detecting and responding to mechanical signals (Fernandes et al., 2018).

Therefore, when velocity profile is laminar, axially symmetric and fully developed, atheroprotective genes are activated, so that normal endothelial are maintained; on the other hand, in case of low and oscillatory shear stress, gene expression is unfavourable, and it leads to endothelial dysfunction. It results that where vessel geometry shapes a disturbed flow, as in branches and curvatures, atherosclerosis onset is promoted, whereas the straight part of arterial tree is generally protected against atherosclerosis (Wasilewski et al., 2013).

From the several studies examined until this point it clearly emerges how hemodynamics and vessel geometry are significant in localizing the sites of plaque formation (Giddens et al., 1993): the detection of the regions of vessels characterized by complex geometry and complex blood flow patterns can be therefore helpful in predicting focal points of the onset of atherosclerosis (Gallo et al., 2015; Giddens et al., 1993; Schulz & Rothwell, 2001).

In recent years, many researchers questioned the strength of low-oscillatory shear theory; in fact, they claim that colocalization of atherosclerotic lesions with areas of low and oscillating WSS may be not as precise as previous literature results could suggest.
In a systematic review, written by Peiffer et. al., the authors (Peiffer et al., 2013a) examined many papers focusing on the correlation between atherosclerotic lesions prevalence and areas of low/oscillating wall shear stress; some of the analysed studies broke the unanimity about low-oscillatory shear theory, therefore defined as "less robust than commonly assumed".

Moreover, a more recent article (Weinberg, 2022) resumed this topic, stressing how controverse is the position about the role of by low and/or oscillatory WSS in triggering the onset of the atheroma. Weinberg suggests that contradictions can be resolved by taking age into account, a factor that changes patterns of permeability and lesion, and that is better explained by transWSS, an indicator of multidirectionality of haemodynamic stresses.

The potential of multidirectionality of haemodynamic stresses (Figure 13) in the onset of the disease in arteries has been recently explored by many other papers (Bailey et al., 2014; Mohamied et al., 2017; Peiffer et al., 2013b). The WSS does not remain parallel to a single axis throughout the cardiac cycle and the direction of WSS could influence the biology of endothelial cells, altering the balance between pro- and anti-atherosclerotic signals. So, the multidirectionality of near-wall flow is thought to be highly pro-atherogenic (Mohamied et al., 2015).

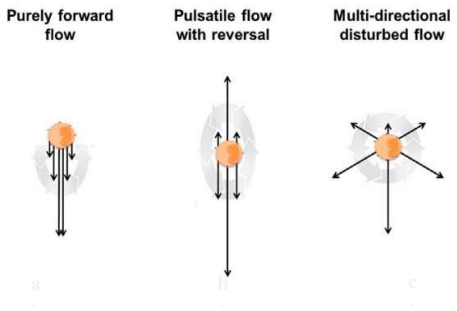

Figure 73. Different patterns of flow: a) purely forward, not pulsatile; b) unidirectional, pulsatile; c) multidirectional

2.7 Carotid bifurcation

In this work, the analysis of hemodynamics will be focused on a specific district of the arterial tree, particularly examined in literature: the carotid bifurcation.

The carotid arteries are major blood vessels, located in the neck, that carry oxygen-rich blood to the brain, head and face (Figure 14).

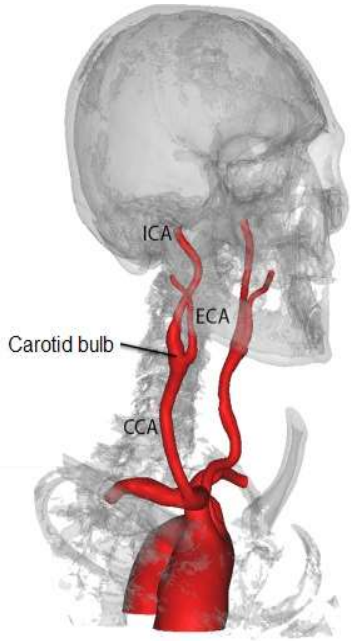

Figure 84. Carotid arteries

There are two carotid arteries, one on the right and one on the left; the right common carotid artery originates in the neck from the brachiocephalic trunk, while the left one arises from the aortic arch in the thorax (Figure 14). Each common carotid artery (CCA) divides itself into two branches (Figure 14, Figure 15) (*Common Carotid Artery - Physiopedia*, n.d.):

- external carotid artery (ECA), that provides blood to the face and neck;
- internal carotid artery (ICA), which supplies blood to the brain.

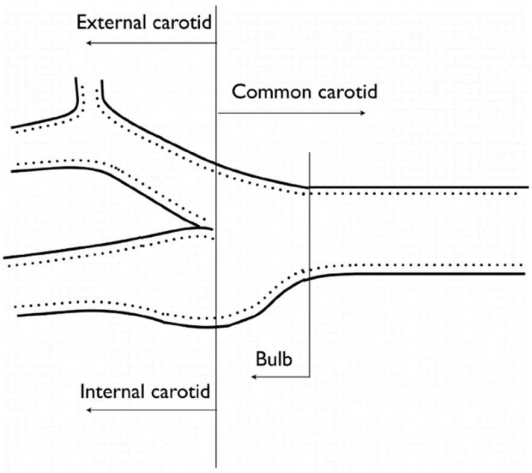

Figure 15. Carotid bifurcation

The branch point is characterized by a dilatation of the vessel, called carotid bulb or carotid sinus, that involves the proximal portion of the ICA and/or the distal region of the CCA (Figure 15).

Since vessel morphology plays a fundamental role in shaping the flow patterns of the blood, it follows that the complicated anatomy of carotid artery leads to asymmetric velocity profiles and flow disturbances.

Figure 16 shows velocity profiles in the carotid.

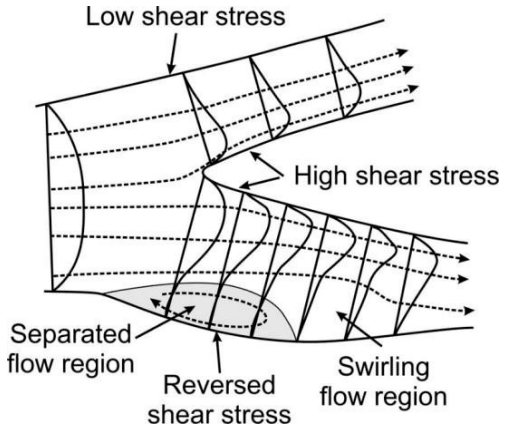

Figure 16. Blood velocity pattern in a carotid bifurcation

The presence of curvatures in a vessel changes the direction of blood flowing in it; a change in momentum is therefore generated, given by the pressure gradient across the vessel cross-section, with higher pressure at the outside of the curve. As a consequence, the fluid near the centreline is driven outwards in the curve, whereas the portion of fluid near the wall, characterized by lower values of velocity, is driven toward the inside of the curve. This sets up a secondary motion in the vessel cross-section, in the form of a pair of counter-rotating axial vortices, one either side of the symmetry plane of the curved vessel (Caro et al., 1992; Motomiya & Karino, 1984). These counter-rotating vortices are called Dean vortices (Dean, 1927). Helical flow has been proven to modify near-wall transport topology, reducing the accumulation of atherogenic substances on the vessel wall and therefore protecting against atherosclerosis (Liu et al., 2014).

Moreover, at the bifurcation, the portion of blood near the centerline - characterized by relatively high velocities - impinges on the flow divider (the surface where the two branches meet). Consequently, the velocity profiles in the branch vessels are markedly asymmetric, with higher velocities and shear stresses in the regions close to the flow divider. Near the walls instead, where the velocities and WSSs are much lower, the streamlines of fluid moving

separate from the wall because of inertia and they reattach at downstream points; consequently, a region of recirculating flow therefore arises, with reversed shear stress at the wall (Secomb, 2016), at the outer wall of the proximal segment and sinus of the ICA.

Summarizing, carotid artery is characterized by disturbed flow conditions and shear distribution at the luminal surface, especially in the carotid bulb and outer wall of the proximal segment and sinus of the ICA (Figure 17); that is the reason why the hemodynamics at the carotid bifurcation has been widely studied because of the preferential development of atherosclerosis (Gallo et al., 2015).

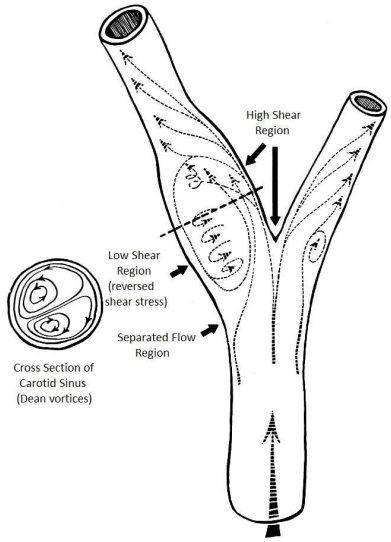

Figure 17. Flow phenomena occurring in a human carotid bifurcation

Chapter 3. Wall Shear Stress Topological Skeleton

In light of the observations described in Chapter 2, low and oscillatory WSS can be considered as significant, but only moderate predictors of localization of atherosclerosis (Morbiducci et al., 2020; Peiffer et al., 2013a; Weinberg, 2022). The complex hemodynamic milieu the endothelium is exposed to can be only partially characterized by low and oscillatory WSS. In this context, to better understand how local hemodynamics and vascular disease are associated, the analysis of WSS vector field topological skeleton has recently been reason for interest (Mazzi et al., 2020; Mazzi, Morbiducci, et al., 2021; Morbiducci et al., 2020).

Given a vector field **u**, the organizing structures of the vector field can be described by the topological skeleton of **u**.

Considering WSS as the vector field and under steady-state conditions - which occur when WSS does not explicitly depend on time - the topological skeleton consists of fixed points, i.e., points where WSS is equal to zero, and the manifolds connecting them (Figure 18) (Mazzi, Morbiducci, et al., 2021).

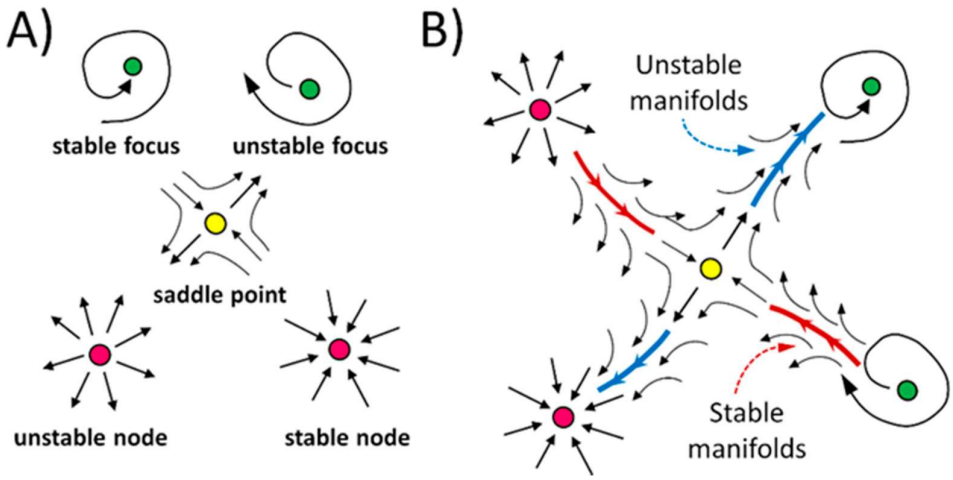

Figure 98. A) Configuration of WSS topological skeleton fixed points: stable/ustable focus, stable/ustable node, saddle point; B) Sketch of the manifolds linking fixed points; stable manifolds in red, unstable in blue.

Specifically, a fixed point (or critical point) is a point where the vector field locally vanishes; it can either attract the nearby trajectories - stable fixed point, therefore characterized by a sink configuration – or repel them - unstable fixed point, therefore characterized by a source configuration (Mazzi et al., 2020). Depending on the way it attracts/repels the

trajectories in its neighbourhood it can be classified as a saddle point, node, or focus (Figure 18):

- A saddle point is a point attracting and repelling nearby trajectories along different directions (i.e., where the streamlines of the vector field intersect themselves).
- A stable/unstable node is characterized by converging/diverging streamlines.
- A focus is characterized by whirling trajectories, and it can be attracting or repelling.

The exact location of fixed points can be found by computing the Poincaré index (Garth et al., 2004), a topological invariant index quantifying how many times a vector field rotates in the neighbourhood of a point.

The Poincaré index is equal to -1 at saddle point locations, 1 at node or focus locations, and 0 otherwise; it therefore allows to identify fixed point locations, but it does not provide information about the fixed points nature (attracting or repelling streamlines).

The classification of fixed points can be performed by calculating the Jacobian matrix of WSS field and computing the eigenvalues of this matrix, as summarized in Table 1.

$\boldsymbol{\lambda}$	**Fixed points**
$\lambda_1 < 0 < \lambda_2$	Saddle point
$\lambda_1, \lambda_2 > 0$	Unstable node
$\lambda_1, \lambda_2 < 0$	Stable node
$\lambda_{1,2} = \alpha \pm \beta i$	Unstable focus
$\lambda_{1,2} = -\alpha \pm \beta i$	Stable focus

Table 1. Classification of fixed points based on the eigenvalues of the Jacobian matrix

The nature (real or complex) and the sign of eigenvalues identify the category of a fixed point. In detail:

- two real eigenvalues with different signs identify a saddle point;
- two real eigenvalues with the same sign identify nodes characterized as attracting or repelling (i.e., stable or unstable, respectively) according to their sign (negative or positive, respectively);
- complex conjugate eigenvalues identify a stable or unstable focus according to the sign of the real part (negative or positive, respectively).

As mentioned before, fixed points are connected by topological spaces called manifolds, which can be either stable or unstable; these manifolds express different behaviour and dynamics of the vector field. In particular, an unstable manifold direct nearby trajectories inwards, as opposed to the stable manifold, which direct them outwards (Figure 18).

In order to identify manifolds of a vector field, two different perspectives have been advanced. One focuses on individual particles, and it tracks their motion along their paths as they are transported by the flow field: it is called Lagrangian perspective. On the other hand, the so-called Eulerian perspective considers the properties of the vector field under analysis at each fixed location in space and time.

For the purpose of this study, we chose to investigate the topological skeleton features using a Eulerian-based approach, whose theoretical background is briefly explained below.

3.1 Eulerian approach: Volume contraction theory and Wall Shear Stress divergence

The Eulerian method is based on the so-called volume contraction theory, which describes the temporal change of an elemental volume dV of a vector field ($\boldsymbol{u}(x,t)$) related to a dynamical system; this element of volume generally evolves during time, and this results in a contraction or expansion of the volume itself

Through mathematical passages, widely explained in (Mazzi, Morbiducci, et al., 2021), it emerges that the rate of volume variation of the vector field $\boldsymbol{u}$ for $dV \to 0$ can be expressed in terms of the local value of vector $\boldsymbol{u}$ divergence.

In light of this, if we apply volume contraction theory to cardiovascular flows, we can perform the analysis of the WSS topological skeleton on the luminal surface of a vessel directly calculating the WSS divergence.

However, divergence - as it is - describes specific directional arrangements of the vectors accounting for both variations in magnitude and in direction; in order to consider solely the contribute of direction, the divergence of the normalized WSS vector field can be used :

$$DIV_W = \nabla \cdot \boldsymbol{WSS}_{norm} = \nabla \cdot \left(\frac{\boldsymbol{\tau}}{|\boldsymbol{\tau}|}\right) \qquad \text{Eq.17}$$

The sign of DIV_W allows to discriminate contraction and expansion regions (Figure 19):

- positive values of DIV_W are referred to expansion regions of WSS, and they can be therefore associated to stable manifolds;
- negative values of DIV_W are referred to contraction regions of WSS, and they can be therefore associated to unstable manifolds.

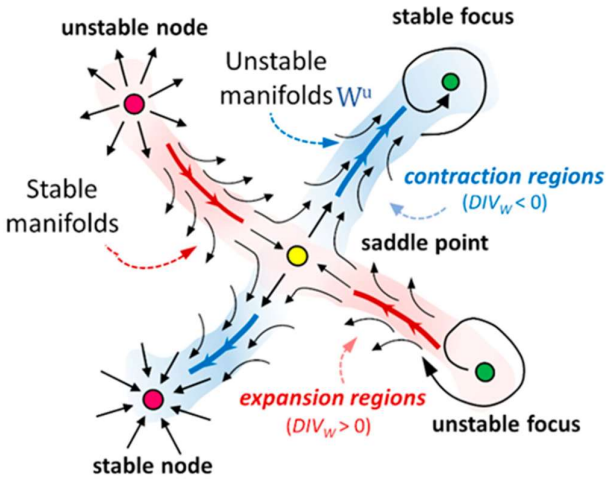

Figure 19. Sketch of the topological skeleton, in which the connection between the sign of normalized divergence of WSS and the nature (stable/unstable) of manifolds is highlighted.

Considering that in cardiocirculatory system WSS is exerted from blood to the endothelial cells layer at the interface, it can be inferred that a local positive value of DIV_W at the luminal surface results in an expansion action of blood flow on the endothelium; on the other hand, a local negative value of DIV_W at the luminal surface results in a contraction action of blood flow on the endothelium (Morbiducci et al., 2020).

Chapter 4. Materials and methods

This study analyses forty-five image-based carotid bifurcation models, investigating some new hemodynamic wall parameters (HWPs) based on the WSS vector field topological skeleton (Mazzi et al., 2020; Mazzi, Morbiducci, et al., 2021; Morbiducci et al., 2020), briefly described in Chapter 3. More specifically, these HWPs are based on the volume contraction/expansion action exerted onto the luminal surface of the vessel, mathematically represented by WSS field divergence.

The purpose of this thesis is to explore if and how these new indicators are linked to the imaging markers of early atherosclerosis at the carotid artery, for the purpose of understanding whether they could be attainable in predicting the onset of this disease. This analysis has therefore been complemented through the evaluation of more traditional indicators, whose correlation with atherosclerosis is well-established.

4.1 Dataset and Computational Fluid Dynamics

The data used for this research form a subgroup selected from the broader VALIDATE (Vascular Aging – The Link that Bridges Age to Atherosclerosis) study. Forty-five ostensibly healthy VALIDATE participants were selected. MRI scans were performed on the right carotid artery of the subjects; in more detail, the protocol included 3D contrast-enhanced magnetic resonance angiography (CE-MRA), phase contrast MRI (PC-MRI) and black blood MRI (BB-MRI) (Gallo et al., 2018).

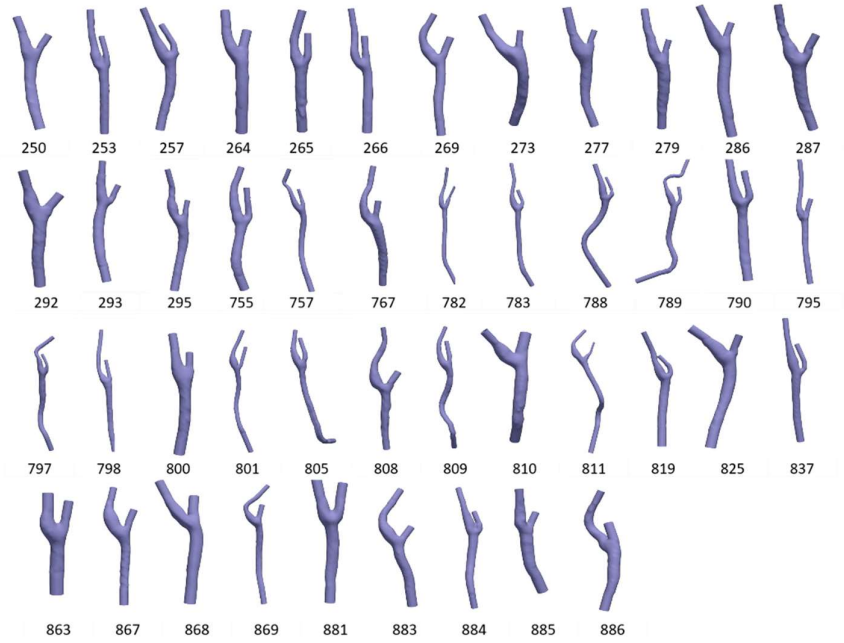

Figure 20 . Synoptic illustration of the geometries of the selected 45 healthy carotid models.

Lumen geometries – illustrated in Figure 20 - were reconstructed using the open-source Vascular Modelling Toolkit VMTK, as described in (Gallo et al., 2015). To ensure fully developed velocity profiles at the CCA inlet and to minimize the influence from outlet boundary conditions, flow extensions were added to the inlet and outlet faces of all models.

To solve the governing equations of the fluid motion, computational fluid dynamic (CFD) simulations have been carried out as described in (Gallo et al., 2018). More in detail, approximately 250 000 quadratic tetrahedral element meshes were generated with a node spacing of 0.25 mm, which was previously shown to successfully resolve wall shear stresses at normal carotid bifurcation geometries (Steinman et al., 2002).

Inlet and outlet velocities were acquired from PC-MRI sequences; this allowed to impose fully developed, pulsatile, patient-specific velocity profile boundary conditions at the CCA inlet and ICA outlet. Traction-free boundary conditions were imposed at the ECA outlet. Rigid walls and Newtonian rheology with constant blood viscosity of 0.00371 kg/m*s were assumed for all models. The CFD simulations were carried out using 4800 time steps per cardiac cycle.

4.2 Imaging markers

The reconstruction of the lumen geometries of the carotid bifurcations from imaging allowed us to obtain important features of the model; in particular, we focused on specific geometric variables, briefly described below, which are proven to be useful to predict early atherosclerosis.

4.2.1 FlareA

The expansion, or flare (Figure 21.A), of a bifurcation is well known to promote flow separation, the consequence of which is low and oscillating shear (Lee et al., 2008; MacLean & Roach, 1998): the wider is the flare, the more disturbed is the flow.
In this study we considered the FlareA variable, that describes the local expansion of the lumen; following the definition in (Bijari et al., 2012), FlareA has been computed as the ratio of the maximum CCA cross-sectional area proximal to the bifurcation flow divider (CCAmax), divided by the CCA3 area (i.e. the luminal area of CCA considered at 3 radii along its length from the bifurcation point). (Figure 21.B).

4.2.2 Tort 2D

Lee et al., in their study in 2008 (Lee et al., 2008), introduced a geometric variable called tortuosity; it expresses the fractional extra distance blood must travel in the real vessel versus a theoretical, straight-line path and in Lee's study it was found to have a significant relationship with disturbed flow (Figure 21.C).
Lee's tortuosity is a three-dimensional variable; in our study we considered instead a second, bidimensional tortuosity variable (Tort2D), defined by (Bijari et al., 2012), that focuses on the planar curvature component, as secondary flows are driven primarily by planar rather than out-of-plane curvature (Figure 21.D).

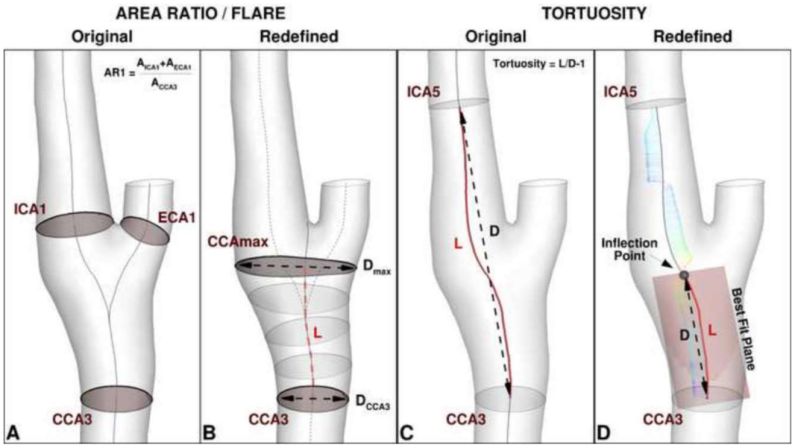

Figure 21. Elements in the definition of geometric variables. In panels A and B, planes normal to the centerlines are used to define the original flare (or area ratio, AR1) and redefined flare (FlareA) variables. In panel C, the thick (red) solid line identifies the centerline segment used to compute the original Tortuosity. In panel D, Tort2D is determined projecting the tortuosity based on the segment identified by the thick (red) line onto the best-fit plane.

4.2.3 Wall thickness

Since artery remodelling is one of the main phenomena that occur with atherosclerosis onset and progression, wall thickness has been widely examined as a surrogate marker for this disease (i.e. (Bijari et al., 2014; de Groot et al., 2004; MacLean & Roach, 1998)).

Besides, many clinical studies using high-resolution magnetic resonance imaging (MRI) have provided indirect evidence in vivo of the influence of

haemodynamics on early wall thickening at the carotid bifurcation (Gallo et al., 2018), influence that this study also aims to ascertain.

To measure wall thickness (WT), the inner and outer wall boundaries were segmented semi-automatically from pre- and post-contrast BB-MRI images.

4.2.4 Contrast enhancement

The earliest preclinical manifestations of atherosclerotic disease, such as endothelial cells (EC) dysfunction and inflammation, appear prior to wall thickening and evident structural changes of the vessel wall. Using contrast enhanced MRI can be significantly helpful to detect them: in fact, the uptake of the gadolinium contrast agent into the wall is mediated mainly by the increased EC permeability associated with EC dysfunction (Gallo et al., 2018). Therefore, an enhanced contrast in CE-MRI imaging can localize a focal endothelial dysfunction.

Contrast enhancement (CE) was computed as the relative change in intensity at the vessel wall from the pre- to post-contrast BB-MRI images.

4.3 Hemodynamic Quantitative Descriptors

Starting from the WSS vector distribution at the surface of the vessel lumen, the WSS topological skeleton was examined; for this purpose, a Eulerian method have been applied (Mazzi et al., 2020). First the topological skeleton of the cycle-average WSS vector field at the luminal surface, then the instantaneous WSS topological skeleton along the cardiac cycle were characterized.

The method we applied relies on the Volume Contraction Theory and it analyses the WSS topological skeleton through the WSS vector field divergence and Poincaré index; the theorical background behind the method has been described in Chapter 3.

WSS manifolds have been encased by the divergence of the normalized WSS vector field ($\boldsymbol{WSS}_{norm}$):

$$DIV_W = \nabla \cdot \boldsymbol{WSS}_{norm} = \nabla \cdot \left(\frac{\boldsymbol{\tau}}{|\boldsymbol{\tau}|}\right) \qquad \text{Eq.17}$$

where $\boldsymbol{\tau}$ is the WSS vector. Positive values of DIV_W are associated to stable manifolds, negative values of DIV_W are associated to unstable manifolds.

The WSS fixed points locations were determined using the Poincaré index. Then, the identified fixed points were classified using the approach based on the eigenvalues of the Jacobian matrix of the WSS vector field: two real eigenvalues with different signs identify a saddle point, two real eigenvalues with the same sign describe a node (attractive/repelling in accordance with the signs), complex conjugate eigenvalues identify a focus node (stable/unstable in accordance with the signs).

In order to quantify the variation in the WSS contraction/expansion action exerted at the carotid luminal surface along the cardiac cycle, the Topological Shear Variation Index (TSVI) has been used; TSVI is defined as the root mean square deviation of the divergence of the normalized WSS vector field with respect to its average over the cardiac cycle:

$$TSVI = \left\{ \frac{1}{T} \int_0^T (DIV_W - \overline{DIV_W})^2 \ dt \right\}^{1/2} \qquad \text{Eq.18}$$

where T is the temporal length of a cardiac cycle, the overbar denotes a cycle-average quantity.

The unsteady nature of the WSS vector field fixed points along the cardiac cycle was characterized using the WSS fixed point weighted residence time ($RT\nabla_{x_{fp}}$) along the cardiac cycle:

$$RT\nabla_{x_{fp}}(e) = \frac{\bar{A}}{A_e} \frac{1}{T} \int_0^T I_e(x_{fp}, t) \, |(\nabla \cdot \boldsymbol{\tau})_e| \ dt \qquad \text{Eq.19}$$

where x_{fp} is the location of a WSS fixed point at time $t \in [0, T]$; T is the cardiac cycle duration; e is the generic triangular element of the superficial mesh of area A_e and $\bar{A}$ is the average surface area of all triangular elements of the superficial mesh of the luminal surface of the vessel, I_e is the indicator function (equal to 1 if $x_{fp} \in e$, 0 otherwise) and $(\nabla \cdot \boldsymbol{\tau})_e$ is the instantaneous WSS divergence value in e, representing the local strength of the contraction/expansion of the WSS around the considered fixed point. $RT\nabla_{x_{fp}}$ quantifies the residence time (expressed as fraction of the cardiac cycle) spent by a fixed point on the mesh element e of the carotid luminal surface.

Simplifying, $RT\nabla_{x_{fp}}(e)$ quantifies the fraction of the cardiac cycle for which in a generic triangle mesh surface element e on the vessel luminal surface there was a fixed point; the residence time have is weighted by the strength of the local contraction/expansion action (Mazzi, Morbiducci, et al., 2021).

To complement the analysis of the WSS topological skeleton, the luminal distribution of Time-Averaged Wall Shear Stress (TAWSS) magnitude along the cardiac cycle was also evaluated; the exposure to low TAWSS values (lower than 0.4 Pa) is in fact widely recognized as a promoter of atherosclerotic disease, stimulating a proatherogenic endothelial phenotype (Chatzizisis et al., 2008). TAWSS can be computed by integrating WSS vector magnitude at the luminal surface over the cardiac cycle (Eq. 20).

$$TAWSS = \frac{1}{T}\int_0^T |\boldsymbol{WSS}|\ dt \qquad \text{Eq. 20}$$

where T is the cardiac cycle period, during which the WSS vector is measured, and t is the time.

4.4 Volume of interest and normalized areas

Each carotid bifurcation model was clipped at CCA, ICA and ECA planes corresponding to 7, 5 and 2 radii along their respective lengths, indicated as CCA7, ICA5 and ECA2 (Figure 22); besides, all models were split into its above-mentioned branches using the open-source Vascular Modeling Toolkit (Vmtk - the Vascular Modelling Toolkit); this step allowed us to perform the analysis not only on the entire model, but also on the single segment (Figure 23).

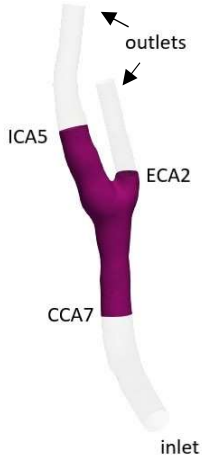

Figure 22. Clipped model (purple) and entire model (white) of a carotid artery bifurcation, with outlet and inlet of the CFD simulation denoted.

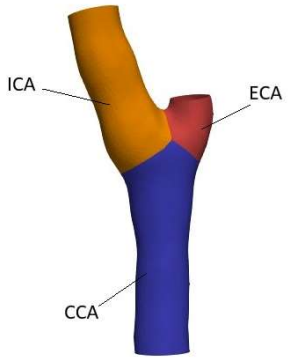

Figure 23. Example of carotid bifurcation model split in its branches: CCA in blue, ICA in orange, ECA in red.

To identify and quantify the luminal surface exposed to proatherogenic hemodynamic conditions, a threshold-based approach have been applied, similarly to the one explained in (Morbiducci et al., 2020). For each carotid model, the values of TSVI, RT and TAWSS associated to each mesh element have been considered and compared to a certain related threshold; if the value was upper (in the case of TSVI and RT) or lower (in the case of TAWSS) than the corresponding threshold, the value has been considered out of the normal range. Then, for each hemodynamic feature, all the areas of mesh elements with out-of-range values have been summed and then divided by a reference area.

In other words, the following normalized areas have been computed:

$$TSVA = \frac{\sum A_{e \mid TSVI(e) > th_{TSVI}}}{A_{ref}} \qquad \text{Eq. 21}$$

$$wFPA = \frac{\sum A_{e \mid RT(e) > th_{RT}}}{A_{ref}} \qquad \text{Eq. 22}$$

$$LSA = \frac{\sum A_{e \mid TAWSS(e) < th_{TAWSS}}}{A_{ref}} \qquad \text{Eq. 23}$$

where e is the mesh element of area A_e , A_{ref} is the reference area, th_{TSVI}, th_{RT} and th_{TAWSS} are the thresholds.

As reference areas - in the denominator of Eq. 21, 22 and 23 -, the total luminal surface of the clipped model or the luminal area of a segment (CCA or ICA) have been considered.

To go into the physical meaning of Eq. 21, 22 and 23:

- Topological Skeleton Variance Area (TSVA) can be defined as the relative surface area exposed to high values of TSVI, and it quantifies the exposure to WSS contraction/expansion action variability.
- Weighted Fixed Points Area (wFPA) consists in the relative surface area exposed to non-null values of $RT\nabla_{x_{fp}}$ and it quantifies the exposure to the action of instantaneous WSS fixed points.
- LSA is the relative surface area exposed to low values of Time-Averaged Wall Shear Stress (TAWSS), whose distribution have been evaluated to complement the WSS topological skeleton characterization.

The following corresponding threshold values have been used:

- TSVA → th_{TSVI} = 80th percentile of the pooled TSVI distribution of the healthy models in the CCA7-ICA5-ECA2 region or in the single segment area (CCA or ICA);
- wFPA → th_{RT} = 0, considering the luminal surface area where fixed points occurred along the cardiac cycle in the CCA7-ICA5-ECA2 region or in the single segment area (CCA or ICA);
- LSA → th_{TAWSS} = 20th percentile of the pooled TAWSS distribution of the healthy models in the CCA7-ICA5-ECA2 region or in the single segment area (CCA or ICA).

To evaluate the strength of the results independently by the area on which the thresholds were computed and by the reference area, different combinations were considered; the resulting variables are listed in Table 2 and 3:

Variable name	**Reference area**	**Thresholds th_{TSVI} = 80th percentile, th_{TAWSS} = 20th percentile, respectively computed on**
TSVA_752		
LSA_752		
TSVA_752_th_cca		
LSA_752_th_cca		
TSVA_752_th_ica		
LSA_752_th_ica		
TSVA_cca_th_752		
LSA_cca_th_752		
TSVA_ica_th_752		
LSA_ica_th_752		
TSVA_cca		
LSA_cca		
TSVA_ica		
LSA_ica		

Table 2. List of the normalized areas obtained by TSVI and TAWSS, with the corresponding reference areas and areas on which respectively 80th and 20th percentile were computed (highlighted in purple).

Variable name	Reference area	Threshold th_{RT} = 0, considered on
wFPA_752		
wFPA_752_th_cca		
wFPA_752_th_ica		
wFPA_cca_th_752		
wFPA_ica_th_752		
wFPA_cca		
wFPA_ica		

Table 3. List of the normalized areas obtained by RT by considering different reference areas and different areas on which RT=0 was computed (highlighted in purple).

The resulting thresholds for TSVI and TAWSS are listed below:

- On CCA7-ICA5-ECA2 region: $th_{TSVI} = 409.61\ m^{-1}$, $th_{TAWSS} = 0.465$ Pa
- On CCA: $th_{TSVI} = 386.82\ m^{-1}$, $th_{TAWSS} = 0.426$ Pa
- On ICA: $th_{TSVI} = 438.24\ m^{-1}$, $th_{TAWSS} = 0.509$ Pa

4.5 Statistical analysis

Bivariate correlations among haemodynamic variables (dependent variables) and imaging markers of early atherosclerosis (independent variables) were determined through the Spearman's rank-order correlation.

Multiple regressions were used for evaluating associations between the combination of hemodynamic variables obtained by different indices (TSVI and TAWSS or TAWSS and RT) versus flare, bidimensional tortuosity, WT or CE. Regressions are reported as the individual coefficient of determination (R^2). For each analysis, significance was assumed for $p<0.05$.

Chapter 5. Results

5.1 WSS Topological skeleton and hemodynamic variables distribution

For the forty-five carotid models examined in this study, the distributions of the considered haemodynamic wall parameters have been reported in Figures from 24 to 27.

5.1.1 Cycle-average WSS Topological skeleton

The cycle-average WSS topological skeleton distribution is presented in Figure 24.

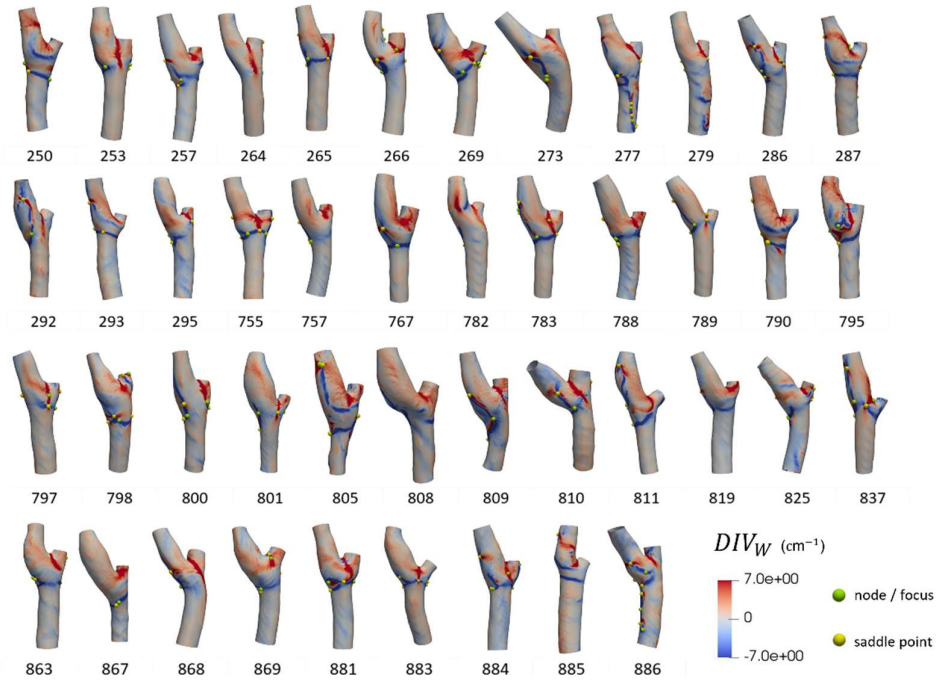

Figure 24. Cycle-average Topological skeleton of WSS vector in the examined pool of 45 healthy carotid models. Blue and red define respectively contraction and expansion regions (unstable/stable manifolds); fixed points are defined in green (nodes or focuses, from where trajectories are attracted or repelled) and yellow (saddle points, intersections of attracting and repelling manifolds).

The results shown in Figure 24 highlight once more the role of geometry in shaping the hemodynamics (Friedman et al., 1983; Malota et al., 2018; Morbiducci et al., 2016) and the distribution of shear stress at the lumen vessel wall. In fact, the variety of configurations of the topological skeleton, in terms of type and localization of both manifolds (stable/unstable) and fixed points (saddle/node/focus), seems to be paired to the geometrical heterogeneity of the carotid models.

Nevertheless, a common trend in the disposition of certain features of WSS topological skeleton can be observed between the models. In fact, carotid sinus and carotid apex appear to be the regions in which manifolds are more frequently located, showing complex patterns of stable and unstable manifolds exerting respectively an expansion or a contraction action onto the endothelial cells. In particular, a WSS expansion region (approximating a stable manifold) is identified around the bifurcation apex as a feature common to all the carotid models (Figure 24).

These results are in the same line as the ones emerged in (Mazzi et al., 2020). In this study, a single carotid bifurcation model from the VALIDATE study have been considered as a representative case, and the cycle-average WSS topological skeleton has been computed (the same type of analysis has been also performed on one intracranial aneurysm model from the Toronto Western Hospital aneurysm clinic). In the considered model - model 755 depicted in Figure 24 - the cycle-averaged fixed points have been mainly found on the carotid bulb, and a persistent saddle point along with an unstable manifold have been observed on the outer wall of the ICA in all the models.

5.1.2 TSVI

The topological shear variation index distribution is presented in Figure 25.

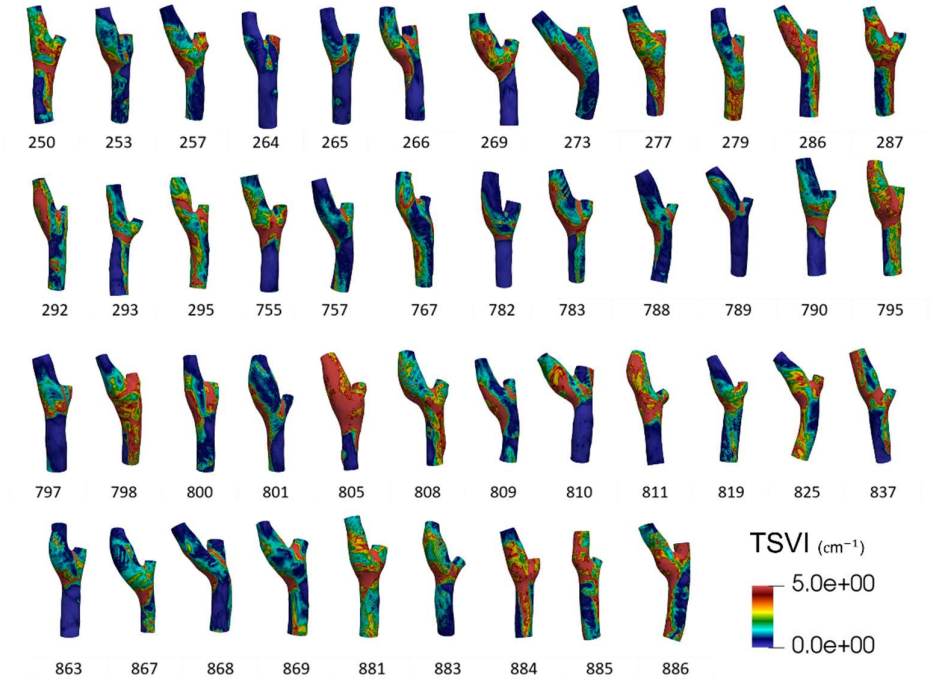

Figure 25. Luminal distribution of Topological Shear Variation Index (TSVI) in the examined pool of 45 healthy carotid models.

As shown by Figure 25, the regions which appear to have higher values of TSVI are the carotid sinus and the entrance of ECA. This is not unexpected, since they are regions particularly characterized by stagnation, recirculation and generally disturbed flow (Secomb, 2016); therefore, variations in the WSS contraction/expansion action exerted at the carotid luminal surface along the cardiac cycle are great in these areas.

5.1.3 TAWSS

The TAWSS distribution is presented in Figure 26.

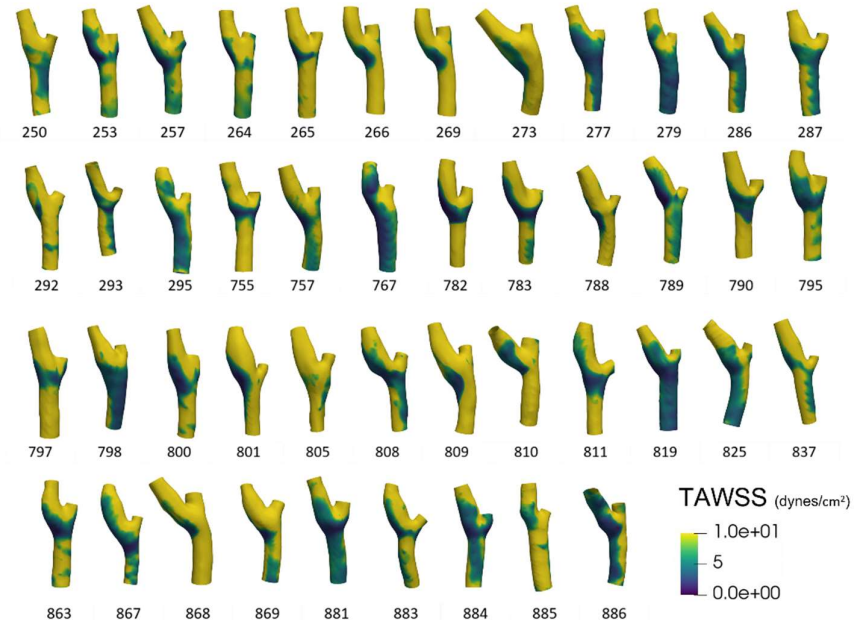

Figure 26. Luminal distribution of Time-Averaged Wall Shear Stress (TAWSS) in the examined pool of 45 healthy carotid models

Figure 26 shows that, as expected, low TAWSS is predominantly located around the outer walls of the bifurcation, and especially at the carotid bulb, where flow separation and blood recirculation occur.

5.1.4 WSS fixed point weighted Residence Time

The WSS fixed point weighted Residence Time distribution is presented in Figure 27.

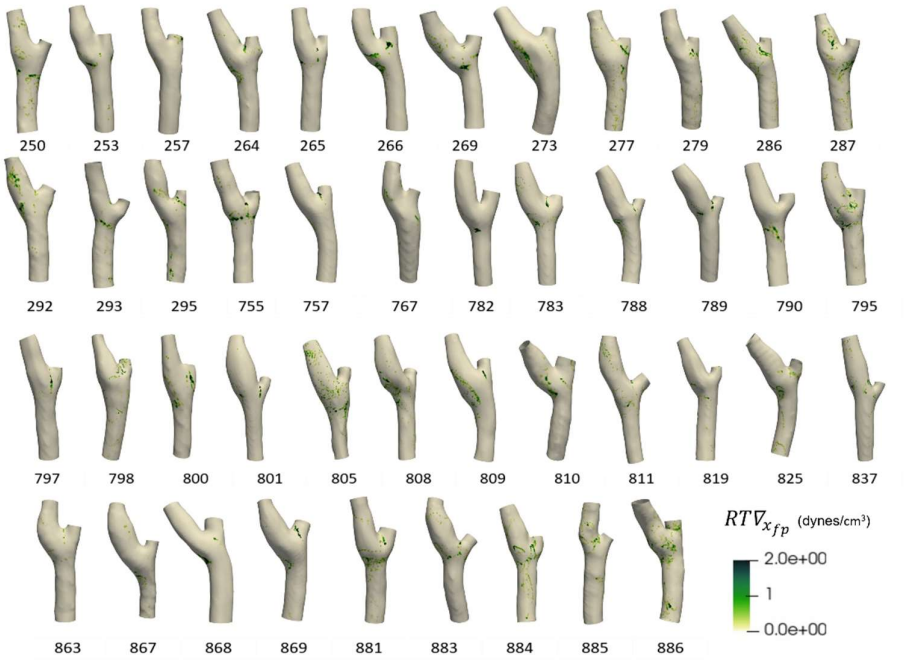

Figure 107. Luminal distribution of WSS fixed points weighted residence time ($RT\nabla_{x_{fp}}$) in the examined pool of 45 healthy carotid models.

The previous results are strengthened by the analysis of the distribution of the $RT\nabla_{x_{fp}}$; in fact, the regions where residence time is greater than zero are mainly located where irregular flow occur, and particularly in the carotid sinus.

Chapter 5. Results

5.1 WSS Topological skeleton and hemodynamic variables distribution

For the forty-five carotid models examined in this study, the distributions of the considered haemodynamic wall parameters have been reported in Figures from 24 to 27.

5.1.1 Cycle-average WSS Topological skeleton

The cycle-average WSS topological skeleton distribution is presented in Figure 24.

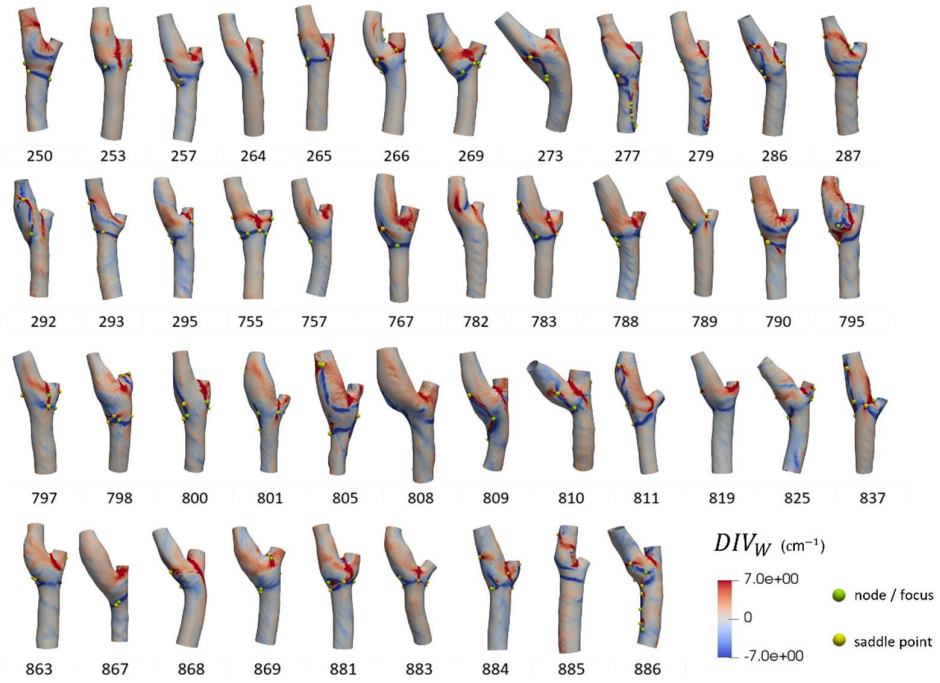

Figure 24. Cycle-average Topological skeleton of WSS vector in the examined pool of 45 healthy carotid models. Blue and red define respectively contraction and expansion regions (unstable/stable manifolds); fixed points are defined in green (nodes or focuses, from where trajectories are attracted or repelled) and yellow (saddle points, intersections of attracting and repelling manifolds).

The results shown in Figure 24 highlight once more the role of geometry in shaping the hemodynamics (Friedman et al., 1983; Malota et al., 2018; Morbiducci et al., 2016) and the distribution of shear stress at the lumen vessel wall. In fact, the variety of configurations of the topological skeleton, in terms of type and localization of both manifolds (stable/unstable) and fixed points (saddle/node/focus), seems to be paired to the geometrical heterogeneity of the carotid models.

Nevertheless, a common trend in the disposition of certain features of WSS topological skeleton can be observed between the models. In fact, carotid sinus and carotid apex appear to be the regions in which manifolds are more frequently located, showing complex patterns of stable and unstable manifolds exerting respectively an expansion or a contraction action onto the endothelial cells. In particular, a WSS expansion region (approximating a stable manifold) is identified around the bifurcation apex as a feature common to all the carotid models (Figure 24).

These results are in the same line as the ones emerged in (Mazzi et al., 2020). In this study, a single carotid bifurcation model from the VALIDATE study have been considered as a representative case, and the cycle-average WSS topological skeleton has been computed (the same type of analysis has been also performed on one intracranial aneurysm model from the Toronto Western Hospital aneurysm clinic). In the considered model - model 755 depicted in Figure 24 - the cycle-averaged fixed points have been mainly found on the carotid bulb, and a persistent saddle point along with an unstable manifold have been observed on the outer wall of the ICA in all the models.

5.1.2 TSVI

The topological shear variation index distribution is presented in Figure 25.

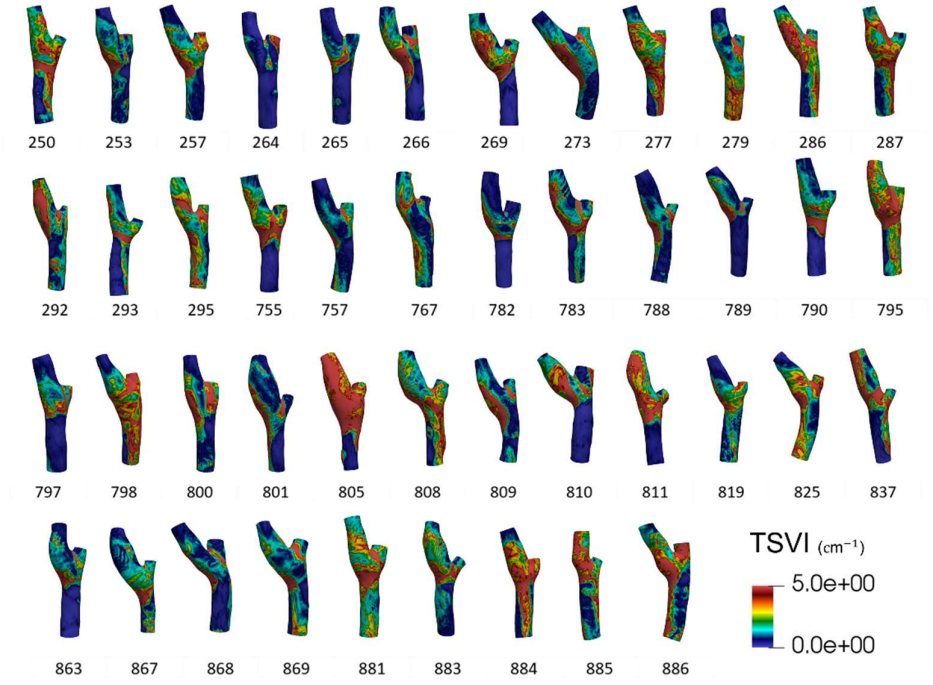

Figure 25. Luminal distribution of Topological Shear Variation Index (TSVI) in the examined pool of 45 healthy carotid models.

As shown by Figure 25, the regions which appear to have higher values of TSVI are the carotid sinus and the entrance of ECA. This is not unexpected, since they are regions particularly characterized by stagnation, recirculation and generally disturbed flow (Secomb, 2016); therefore, variations in the WSS contraction/expansion action exerted at the carotid luminal surface along the cardiac cycle are great in these areas.

5.1.3 TAWSS

The TAWSS distribution is presented in Figure 26.

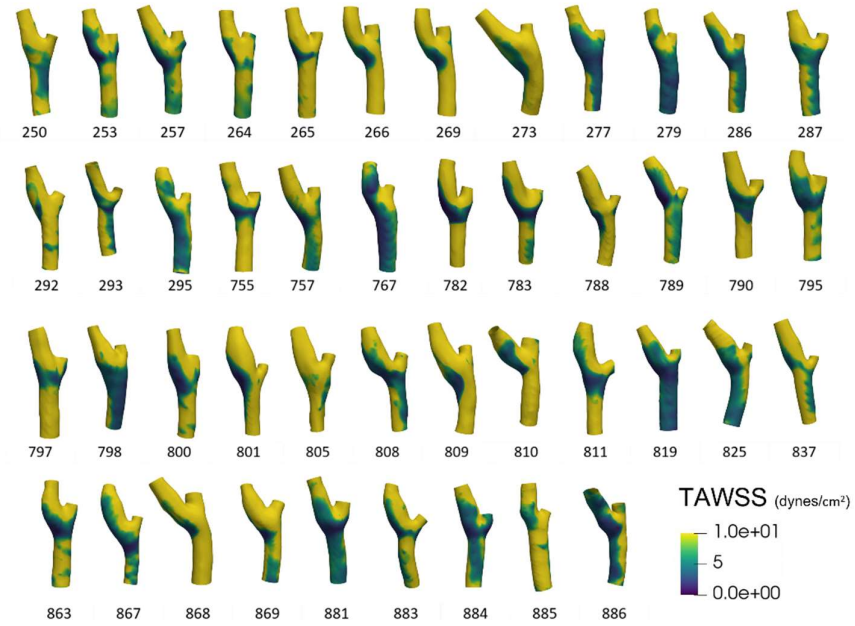

Figure 26. Luminal distribution of Time-Averaged Wall Shear Stress (TAWSS) in the examined pool of 45 healthy carotid models

Figure 26 shows that, as expected, low TAWSS is predominantly located around the outer walls of the bifurcation, and especially at the carotid bulb, where flow separation and blood recirculation occur.

5.1.4 WSS fixed point weighted Residence Time

The WSS fixed point weighted Residence Time distribution is presented in Figure 27.

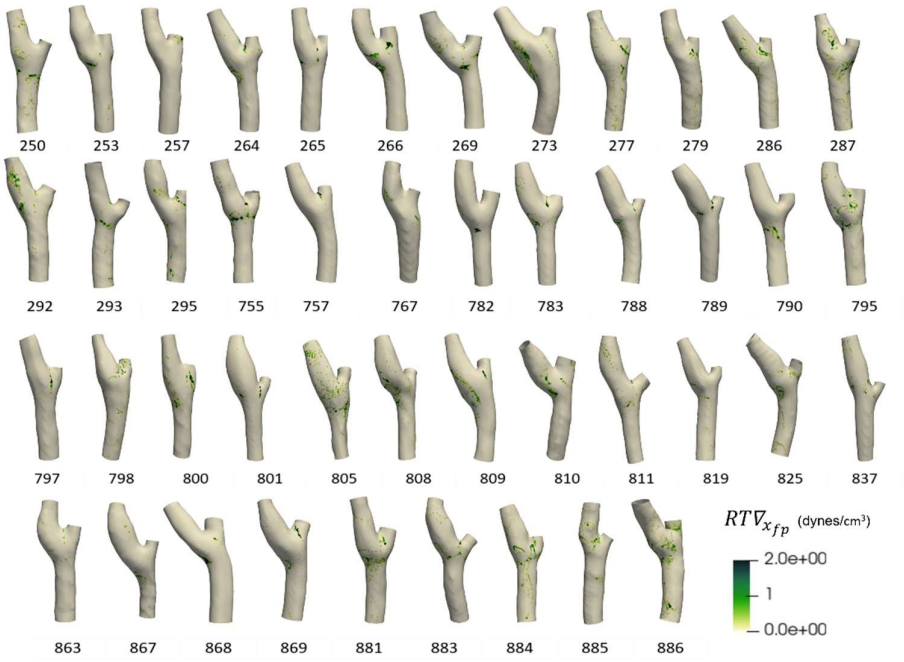

Figure 117. Luminal distribution of WSS fixed points weighted residence time ($RT\nabla_{x_{fp}}$) in the examined pool of 45 healthy carotid models.

The previous results are strengthened by the analysis of the distribution of the $RT\nabla_{x_{fp}}$; in fact, the regions where residence time is greater than zero are mainly located where irregular flow occur, and particularly in the carotid sinus.

5.1.5 Normalized areas: TSVA and LSA

In order to identify the most atherosusceptible luminal surface regions in our carotid models, the normalized areas TSVA, LSA and wFPA have been computed.

Since in wFPA the threshold is equal to zero, the riskiest area in terms of atherosclerosis onset is already described by the green area in Figure 27, which shows the distributions of RT; in this case, its visual representation would not add any further information.

TSVA and LSA are shown in Figures 28 and 29.

5.1.5.1 TSVA

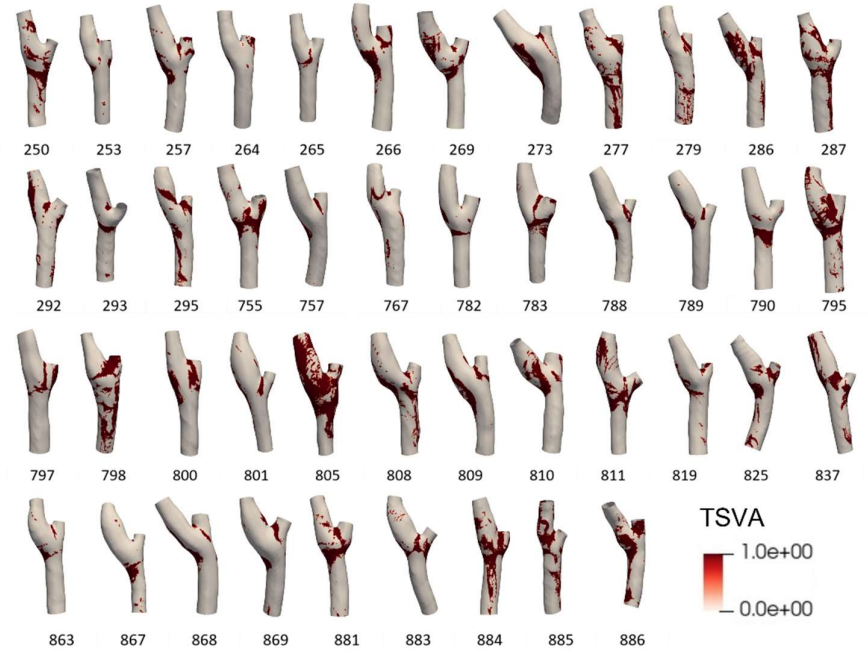

Figure 28. Luminal surface area (in red) exposed to high Topological Shear Variation Index (TSVI), as expressed by its normalized area TSVA, in the examined pool of 45 healthy carotid models. In the shown distributions, the whole area of the clipped model (CCA 7- ICA 5-ECA 2) have been used both as reference area and as area on which threshold (80th percentile value) have been computed.

Comparing Figure 28 with figure 27, a colocalization can be observed between luminal surface areas exposed to $RT\nabla_{x_{fp}}$ greater than 0 and high TSVI in all models, with the latter largely enclosing the former. This is consistent with the fact they both express features of the WSS Topological Skeleton - although the different physical of the two descriptors: the first one expresses the values of the residence time of a fixed point, weighted by the local WSS contraction/expansion action; the second, the normalized WSS divergence variability. This result is in line with (Morbiducci et al., 2020); in this study, the same dataset has been used as a reference healthy cohort, compared to pre and post intervention Carotid Bifurcation Endarterectomy groups of patients; from statistical analysis, a significant association between wFPA and TSVA emerged in all three cohorts, according to the theory.

5.1.5.2 LSA

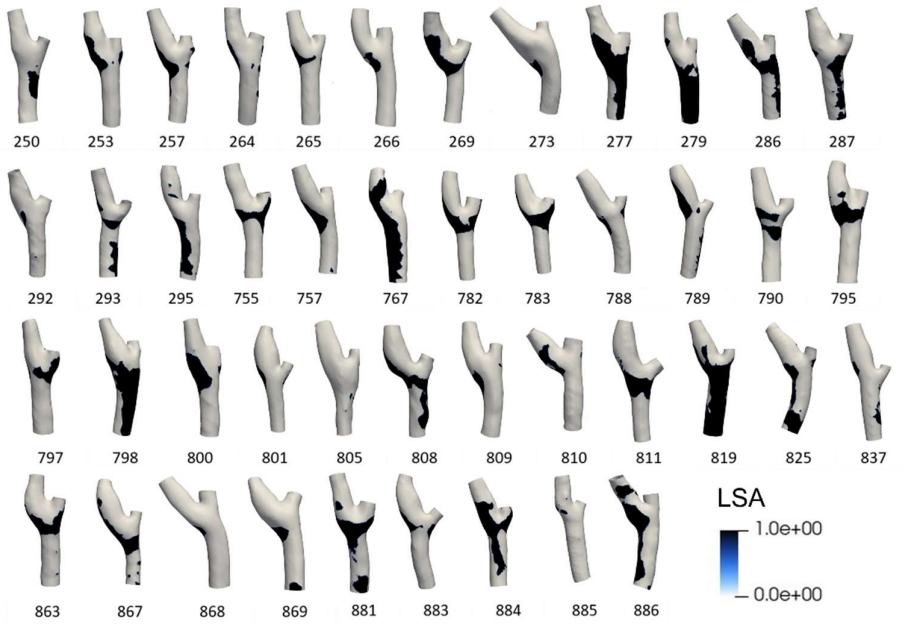

Figure 29. Luminal surface area (in blue) characterized by low Time-Averaged Wall Shear Stress (TAWSS), as expressed by the Low Shear Area (LSA), in in the examined pool of 45 healthy carotid models. In the shown distributions, the whole area of the clipped model (CCA 7- ICA 5-ECA 2) have been used both as reference area and as area on which threshold (20^{th} percentile value) have been computed.

As previously explained, LSA have been computed to complement the WSS topological skeleton analysis. Comparing figure 29 with figure 28, a decent colocalization of the most critical areas can be observed. However, in all models, LSAs include regions not belonging to TSVAs, and vice versa; as previously proven by literature (Morbiducci et al., 2020), TSVI and TAWSS are statistically independent indicators, and so they provide different information about the localization of early atherosclerosis. This independence is valid also in relation to RT, and it is particularly evident comparing LSAs with the green areas characterized by RT>0 in figure 27; in this case, the overlappable areas are even fewer than in the TSVA/LSA comparison.

Also in this case, these results are coherent with the outcome of the statistical analysis performed in (Morbiducci et al., 2020) between normalized areas of hemodynamic descriptors. LSA was not associated to either wFPA or TSVI; Morbiducci (2020) therefore infers that WSS topological skeleton descriptors represent statistically independent variables with respect to the commonly adopted exposure to low TAWSS as a main indicator of disturbed shear in arteries.

5.2 Correlations between hemodynamic variables and imaging markers

5.2.1. Bivariate analysis

In the following graphs, the statistically significant correlations - emerged from bivariate analysis - between image markers and hemodynamic variables are illustrated. The respective coefficient of determination (R^2) and *p* value are displayed below each image. The results are presented examining each considered geometrical variable, and the color maps of Figures 27, 28 and 29 are recalled, in order to label the correlations with hemodynamic variables respectively related to TSVI, $RTV_{x_{fp}}$ and TAWSS.

- **FlareA**
  FlareA has found to be significantly correlated with one hemodynamic variable; this variable consists in the TSVA computed using the whole clipped model as reference area and the 80th percentile of the distribution of TSVI values of the ICA as threshold. The correlation is however quite weak; in fact, the value is very close to 0.05 and the coefficient of determination value is very low.

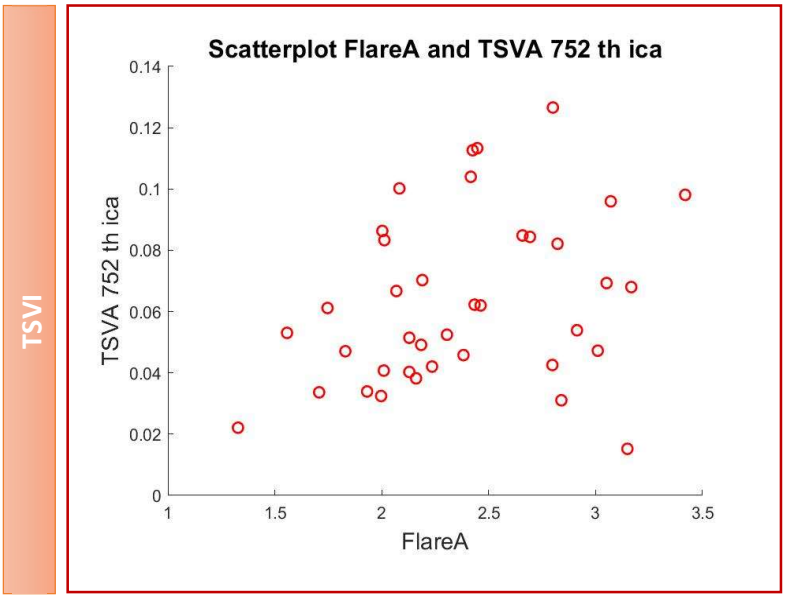

- **Wall thickness**
  From the statistical analysis emerges a significative correlation between the maximum and average value of wall thickness on CCA and hemodynamic variables linked to WSS topological skeleton, considering different reference areas and thresholds. In particular, the correlations between the maximum value of WT in the CCA and the hemodynamic variables TSVA 752, TSVA 752 th cca and wFPA cca th 752 are noteworthy, since their *p* value is smaller than 0.01.

➢ MaxCCA WT:

TSVI

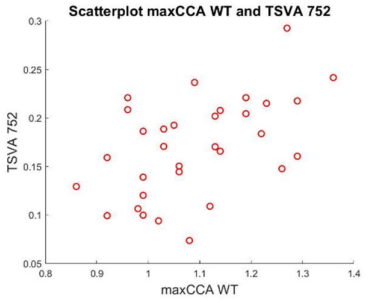

R2 = 0,229774	Pvalue = 0,005505*

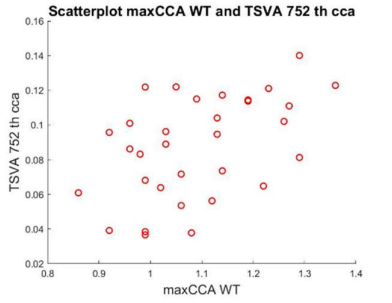

R2 = 0,211834	Pvalue = 0,008035*

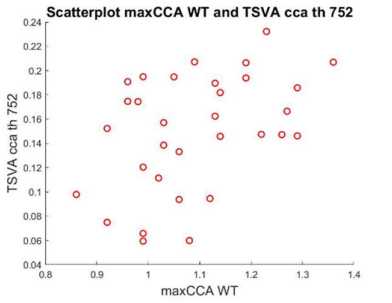

R2 = 0,135763	Pvalue = 0,037983

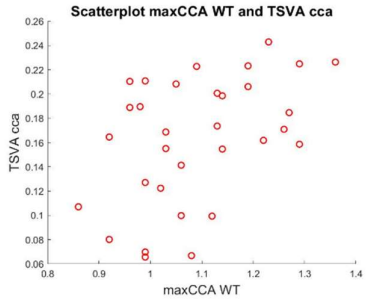

R2 = 0,17048	Pvalue = 0,01884

RT

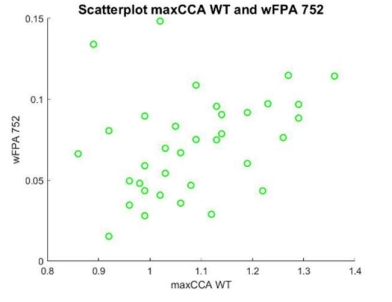

R2 = 0,164065	Pvalue = 0,015789

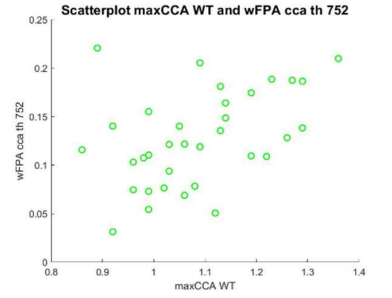

R2 = 0,200443	Pvalue = 0,007929*

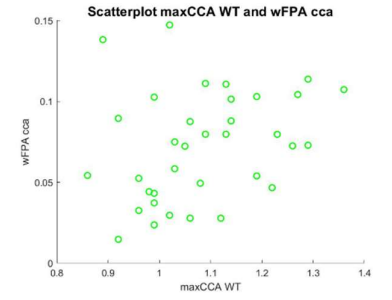

R2 = 0,122451	Pvalue = 0,039332

- MeanCCA WT

TSVI

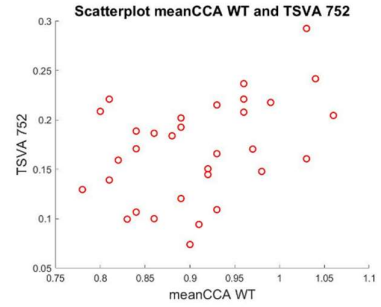

R2 = 0,137851	Pvalue = 0,036423

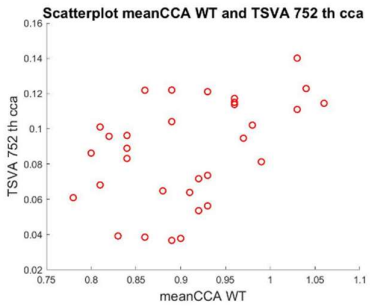

R2 = 0,180384	Pvalue = 0,015396

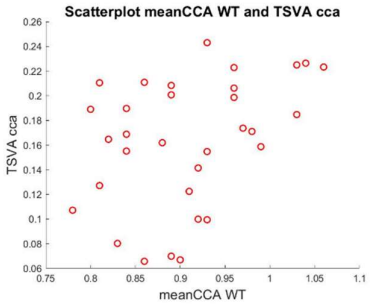

R2 = 0,13433	Pvalue = 0,03909

RT

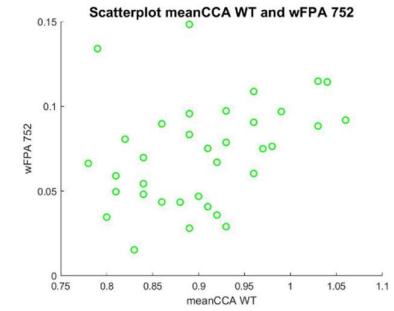

R2 = 0,15614	Pvalue = 0,018807

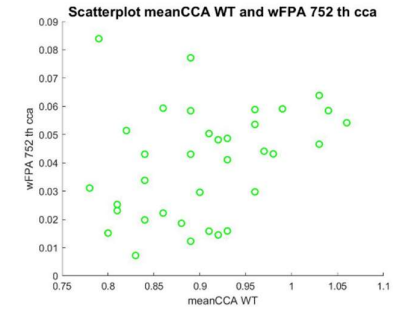

R2 = 0,123754	Pvalue = 0,03823

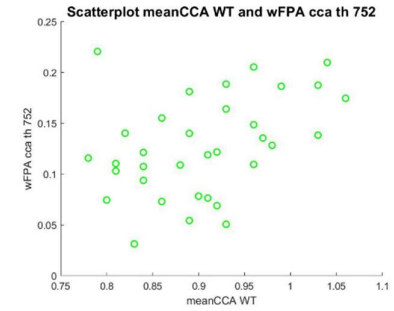

R2 = 0,165333	Pvalue = 0,017015

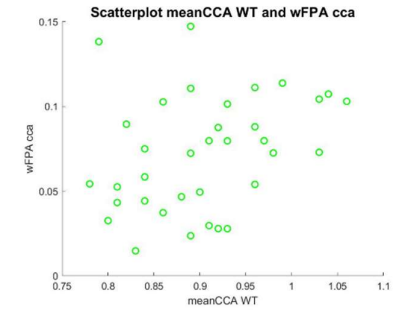

R2 = 0,121102	Pvalue = 0,040507

- **Contrast enhancement**

  From the statistical analysis a significative correlation emerges between maximum and average contrast enhancement value on the ICA and haemodynamic variables related to low WSS, considering different reference areas and different thresholds. In particular, the correlations between the maximum and average value of CE in the ICA and the hemodynamic variable LSA 752 th ica are noteworthy, since their p value is smaller than 0.01.

  ➢ MaxICA CE8

TAWSS

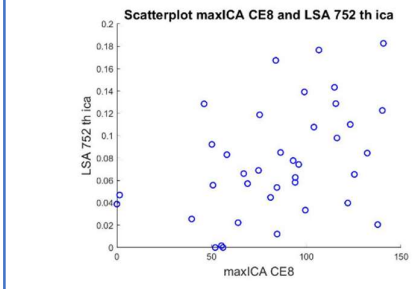

R2 = 0,180731	Pvalue = 0,007799*

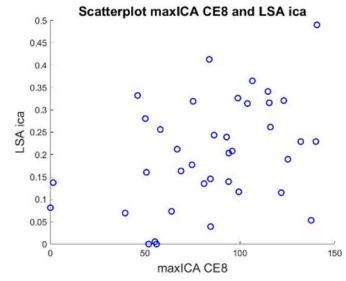

R2 = 0,13575	Pvalue = 0,02284

  ➢ MeanICA CE8

TAWSS

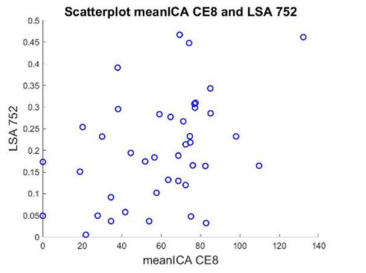

R2 = 0,136422	Pvalue = 0,017473

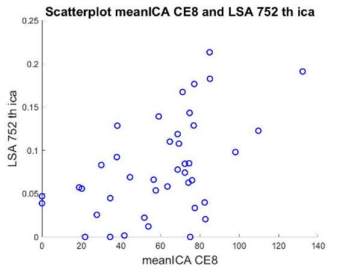

R2 = 0,225558	Pvalue = 0,001703*

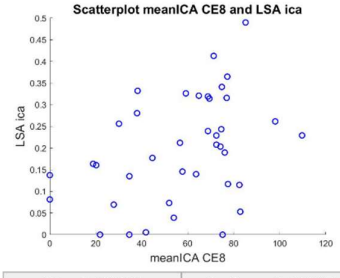

R2 = 0,11904	Pvalue = 0,03147

These significant correlations conform to the outcomes shown in (Gallo et al., 2018), in which the same dataset has been investigated with the purpose of exploring the associations between local haemodynamic and imaging markers of early atherosclerosis. Also in this paper emerges that CE at the carotid bulb (ICA) is significantly associated with low WSS, and no significant association onto the CCA have been found.

We can explain this phenomenon considering the relation between hemodynamics and the pathophysiology of atherosclerosis. In fact, as explained in Chapter 2, the shear stress that the blood flow exerts onto the endothelial cells gives them directionality (in the direction of the flow) and compactness; so low shear stress, along with oscillatory shear stress, contributes to an enhancement in permeability of the endothelium (Wasilewski et al., 2013), which can be observed in MRI imaging through the CE analysis.

- **Tort2D**
  From our statistical analysis, no significant correlation has been found between Tort2D and hemodynamic variables, neither the ones linked to TSVI and RT, nor the ones related to TAWSS.

5.2.2. Multivariate analysis

In the following graphs, the statistically significant correlations resulting from the multivariate analysis are shown. The respective coefficient of determination (R^2) and *p* values are displayed below each image. In particular, three *p* values have been considered for each correlation: the total p value and the two p values related to the single hemodynamic feature. The p values have been named as follows:

- Px1 = pvalue related to TSVA
- Px2 = pvalue related to LSA
- Px3 = pvalue related to wFPA

As the bivariate analysis results, the ones emerged from multivariate analysis are displayed examining each considered geometrical variable, and the color maps of Figures 27, 28 and 29 are recalled to mark the correlations with hemodynamic variables respectively related to TSVI, $RT\nabla_{x_{fp}}$ and TAWSS.

- **FlareA**

  From multiple regression, no significant correlation between FlareA and hemodynamic variables - neither the variables related to TSVI and $RT\nabla_{x_{fp}}$, nor the ones related to TAWSS - surfaced.

- **Wall thickness**

  The multivariate analysis brought to light a phenomenon of shielding of the total p value by the p value associated to TSVA in relation to the one associated to TAWSS. This supports the strength of the correlation between wall thickness on the CCA and WSS Topological skeleton descriptors, considering different reference areas and thresholds. In particular, the role of TSVA 752 in the correlation between the maximum value of WT in the CCA and the hemodynamic variables TSVA 752 and LSA 752 is noteworthy, since its p value is smaller than 0.01.

- MaxCCA WT:

TAWSS

TSVI

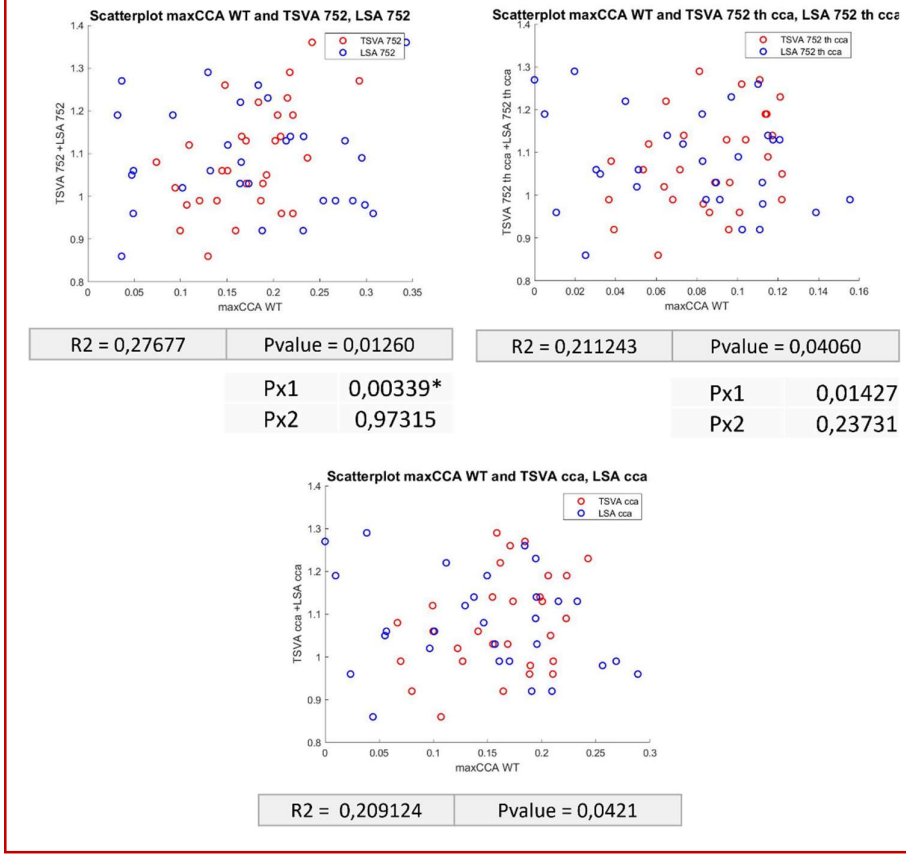

R2 = 0,27677	Pvalue = 0,01260
Px1	0,00339*
Px2	0,97315

R2 = 0,211243	Pvalue = 0,04060
Px1	0,01427
Px2	0,23731

R2 = 0,209124	Pvalue = 0,0421

- MeanCCA WT

TAWSS

TSVI

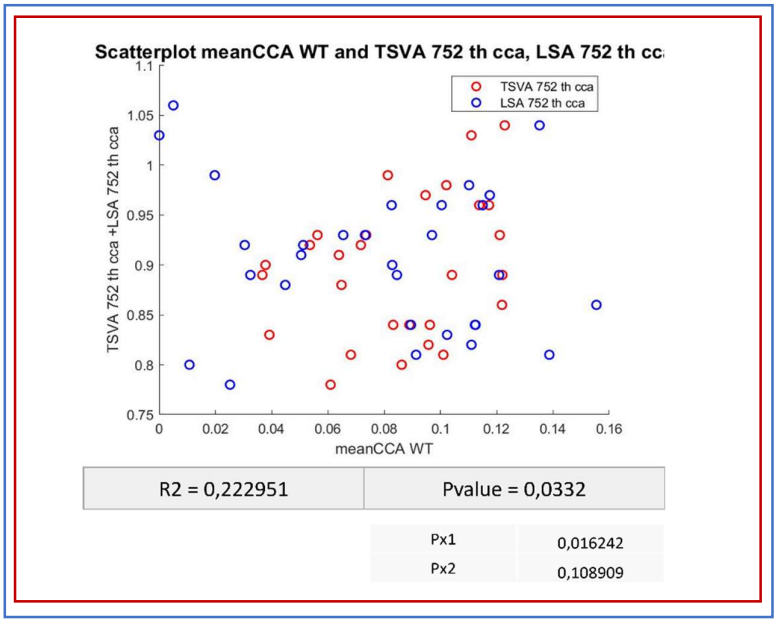

R2 = 0,222951	Pvalue = 0,0332
Px1	0,016242
Px2	0,108909

- **Contrast enhancement**

  From the multiple regression analysis, we can observe a phenomenon of shielding of the total p value by the p value associated to TAWSS, in relation to the ones associated to TSVI or RT. This confirms the strength of the correlation between contrast enhancement on the ICA and low TAWSS, considering different reference areas and thresholds. In particular, the role of LSA 752 th ica in the correlations between the average value of CE in the ICA and the following pairs of hemodynamic variables:
  - TSVA 752 th ica and LSA 752 th ica
  - LSA 752 th ica and WFPA 752 th ica
  is noteworthy, since its p value is smaller than 0.01.

  - MaxICA CE8

TAWSS

TSVI

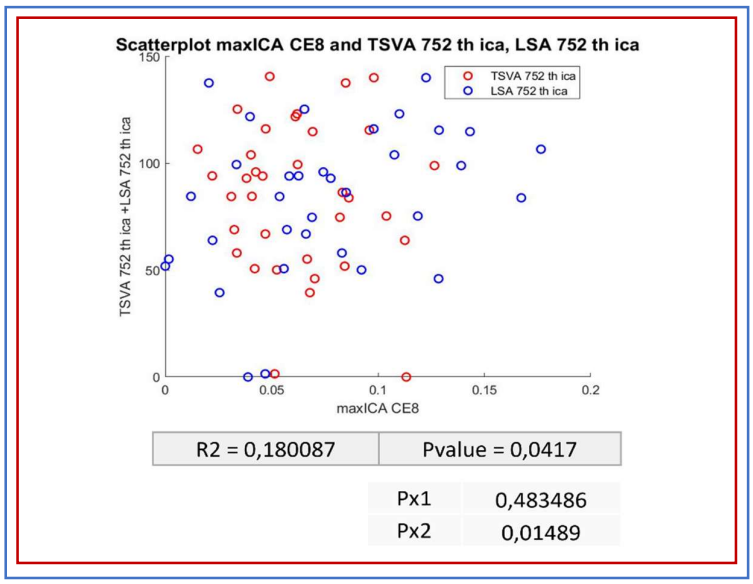

R2 = 0,180087	Pvalue = 0,0417

Px1	0,483486
Px2	0,01489

RT

TAWSS

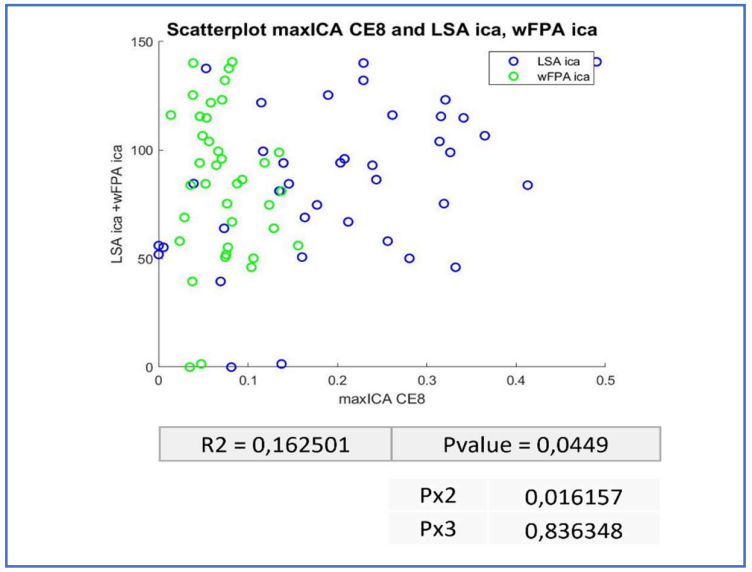

R2 = 0,162501	Pvalue = 0,0449

Px2	0,016157
Px3	0,836348

- MeanICA CE8

TAWSS

TSVI

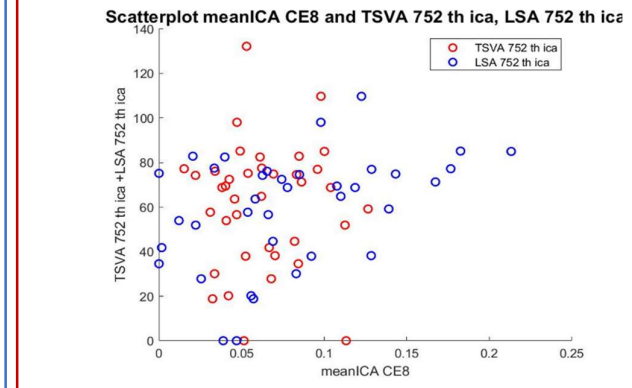

R2 = 0,237375	Pvalue = 0,00872

Px1	0,686572
Px2	0,002231*

RT

TAWSS

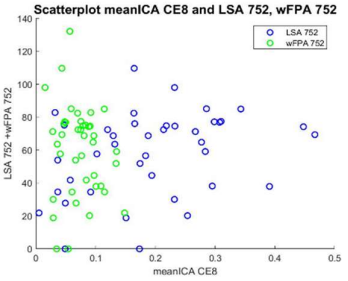

R2 = 0,177509	Pvalue = 0,0244

Px2	0,010029
Px3	0,450895

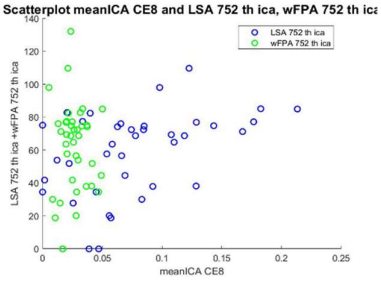

R2 = 0,249902	Pvalue = 0,00565*

Px2	0,001419*
Px3	0,997197

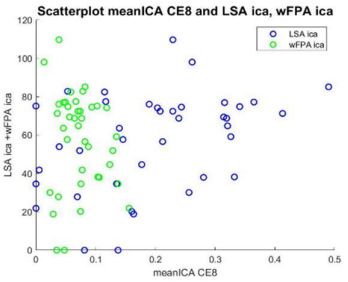

R2 = 0,155189	Pvalue = 0,048

Px2	0,021302
Px3	0,679968

Moreover, statistically significant correlations have been also found between the maximum value of contrast enhancement on the CCA and high TSVI, considering different reference areas and thresholds; from all these correlations emerges that TSVI-related variables have a shielding effect on the total p value, with p values to a great extent smaller than 0.01.

- MaxCCA CE8

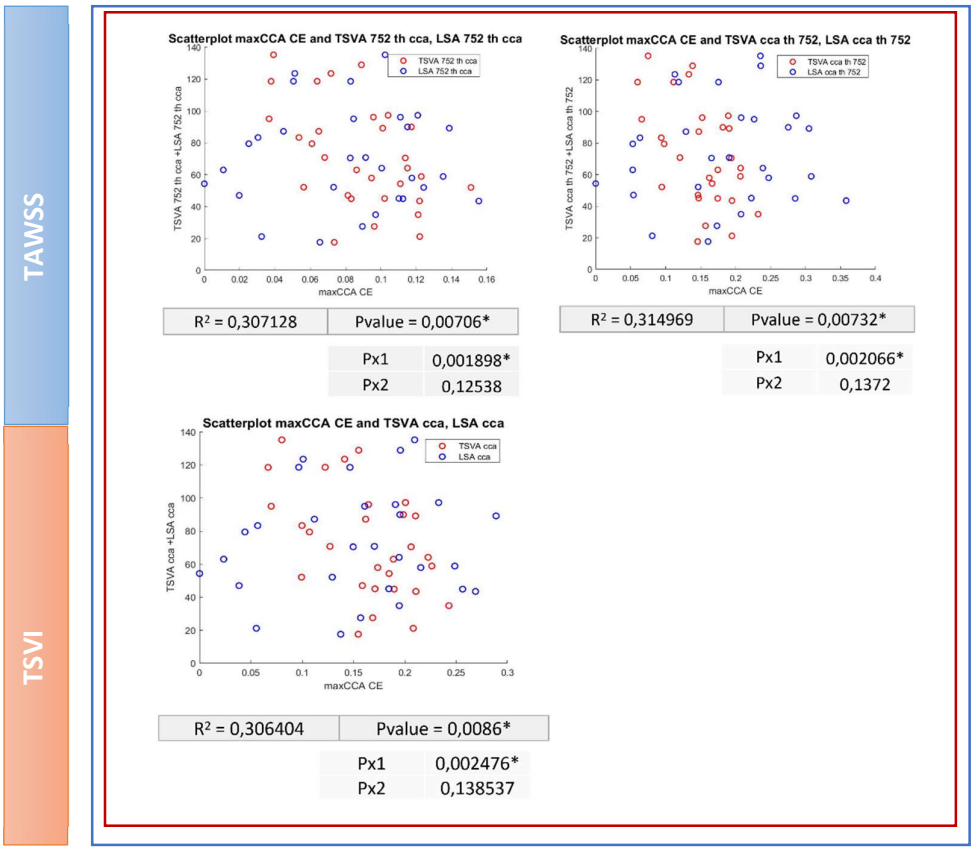

- **Tort2D**

  From our multivariate statistical analysis, no significant correlation between Tort2D and hemodynamic variables - neither the variables related to TSVI and RT, nor the ones related to TAWSS - has been found.

Chapter 6. Conclusions

In short, this study examined how effectively WSS Topological Skeleton features can predict early atherosclerosis onset: to do this, we considered 45 image-based healthy carotid artery models, on which we investigated the associations between WSS Topological Skeleton descriptors and specific imaging markers, which are already considered well-known predictors of the onset of this disease (Bijari et al., 2012; Gallo et al., 2018; Lee et al., 2008; MacLean & Roach, 1998).

The distributions of cycle-average WSS Topological Skeleton and WSS Topological Skeleton descriptors onto the luminal surface of the carotid artery models suggest that WSS Topological Skeleton features could be effective in localizing the most atherosusceptible regions of the bifurcations, in addition to the well-established low WSS.
However, the difference in the physical meaning and the moderate, but not insignificant discrepancies between the respective normalized areas support the thesis that WSS topological skeleton features and low WSS represent different hemodynamic stimuli, possibly impacting differently the vascular response (Morbiducci et al., 2020).

Moreover, the results of the statistical analysis confirm that WSS topological skeleton features are associated to markers of vascular disease, as inferred by previous studies (de Nisco et al., 2020; Mazzi, de Nisco, et al., 2021; Mazzi et al., 2020; Morbiducci et al., 2020). In more detail, positive strong associations have been found between wall thickness (WT) and WSS Topological Skeleton descriptors (both TSVI and RT) on CCA**.** Furthermore, positive strong associations also emerged between contrast enhancement (CE) and low Wall Shear Stress on the ICA, as already found in literature (Gallo et al., 2018).

Only a single, weak association have been found between Flare A and hemodynamic descriptors, on the ICA, and no significant association have been found with Tort2D. This is coherent with the results found in (Gallo et al., 2018) and it diverts from (Bijari et al., 2012), in which these two geometric variables are indicated as promising surrogate markers of local hemodynamics. However, we must consider that in (Bijari et al., 2012), unlike our study:

- not the descriptors separately, but the combination of the two indices have been investigated, since multiple regression have been performed;
- the clipped model used is CCA3, ICA5 and ECA2, involving a shorter portion of CCA than in our models (CCA7, ICA5 and ECA2).

The use of respectively 7 radii rather than 3 radii length of CCA and the employment of different reference areas and thresholds could also have a role in the differences found between our outcomes and the ones found in (Morbiducci et al., 2020). Hence, it could be an interesting exploring the impact of choosing different lengths of CCA in clipped carotid models in the WSS Topological Skeleton and statistical analysis.

Besides, this work focuses only on the near-wall hemodynamic descriptors, not considering the intravascular flow features, e.g. the helicity of the blood flow going through into the

vessels and the vortex structures dynamics ; for this reason, future studies investigating the associations between wall descriptors and bulk flow descriptors are encouraged.

References

Bibliography

Ayyaswamy, P. S. (2016). Introduction to Biofluid Mechanics. In *Fluid Mechanics* (pp. e1–e73). Elsevier. https://doi.org/10.1016/b978-0-12-405935-1.00016-2

Azuma, T., & Hasegawa, M. (1973). Distensibility of the vein: from the architectural point of view. *Biorheology*, *10*(3), 469–479. https://doi.org/10.3233/BIR-1973-10323

Bailey, E. L., Peiffer, V., Mohamied, Y., Chooi, K. Y., Rowland, E. M., Sherwin, S. J., & Weinberg, P. D. (2014). Spatial correlation between patterns of wall permeability and patterns of multidirectional disturbed blood flow in rabbit aorta. *Atherosclerosis*, *232*(2), e2. https://doi.org/10.1016/J.ATHEROSCLEROSIS.2013.11.002

Ballermann, B. J., Dardik, A., Eng, E., & Liu, A. (1998). Shear stress and the endothelium. *Kidney International, Supplement*, *54*(67). https://doi.org/10.1046/j.1523-1755.1998.06720.x

Bijari, P. B., Antiga, L., Gallo, D., Wasserman, B. A., & Steinman, D. A. (2012). Improved Prediction of Disturbed Flow via Hemodynamically-Inspired Geometric Variables. *Journal of Biomechanics*, *45*(9), 1632. https://doi.org/10.1016/J.JBIOMECH.2012.03.030

Bijari, P. B., Wasserman, B. A., & Steinman, D. A. (2014). Carotid Bifurcation Geometry is an Independent Predictor of Early Wall Thickening at the Carotid Bulb. *Stroke; a Journal of Cerebral Circulation*, *45*(2), 473. https://doi.org/10.1161/STROKEAHA.113.003454

Camasão, D. B., & Mantovani, D. (2021). The mechanical characterization of blood vessels and their substitutes in the continuous quest for physiological-relevant performances. A critical review. *Materials Today Bio*, *10*, 100106. https://doi.org/10.1016/J.MTBIO.2021.100106

Caro, C. G., Dumoulin, C. L., Graham, J. M. R., Parker, K. H., & Souza, S. P. (1992). *Secondary Flow in the Human Common Carotid Artery Imaged by MR Angiography*. http://biomechanical.asmedigitalcollection.asme.org/

Chatzizisis, Y. S., Jonas, M., Coskun, A. U., Beigel, R., Stone, B. v., Maynard, C., Gerrity, R. G., Daley, W., Rogers, C., Edelman, E. R., Feldman, C. L., & Stone, P. H. (2008). Prediction of the localization of high-risk coronary atherosclerotic plaques on the basis of low endothelial shear stress-an intravascular ultrasound and histopathology natural history study. *Circulation*, *117*(8), 993–1002. https://doi.org/10.1161/CIRCULATIONAHA.107.695254

Chaudhry, R., Miao, J. H., & Rehman, A. (2022). *Physiology, Cardiovascular*.

Chien, S. (1970). Shear Dependence of Effective Cell Volume as a Determinant of Blood Viscosity. *Science*, *168*(3934), 977–979. https://doi.org/10.1126/SCIENCE.168.3934.977

de Groot, E., Kees Hovingh, ; G, Wiegman, A., Duriez, P., Andries, ;, Smit, J., Fruchart, J.-C., & Kastelein, J. J. P. (2004). *Measurement of Arterial Wall Thickness as a Surrogate Marker for Atherosclerosis From the Department of Vascular Medicine (E*. https://doi.org/10.1161/01.CIR.0000131516.65699.ba

de Nisco, G., Tasso, P., Calò, K., Mazzi, V., Gallo, D., Condemi, F., Farzaneh, S., Avril, S., & Morbiducci, U. (2020). Deciphering ascending thoracic aortic aneurysm hemodynamics in

relation to biomechanical properties. *Medical Engineering & Physics*, *82*, 119–129. https://doi.org/10.1016/J.MEDENGPHY.2020.07.003

Dean, W. R. (1927). Fluid Motion in a Curved Channel. *Proceedings of the Royal Society of London, Series A*, *121*(787), 402–420. https://royalsocietypublishing.org/

Dessalles, C. A., Leclech, C., Castagnino, A., & Barakat, A. I. (2021). Integration of substrate- and flow-derived stresses in endothelial cell mechanobiology. In *Communications Biology* (Vol. 4, Issue 1). Nature Research. https://doi.org/10.1038/s42003-021-02285-w

dos Santos, V. P., Pozzan, G., Castelli Júnior, V., & Caffaro, R. A. (2021). Arteriosclerosis, atherosclerosis, arteriolosclerosis, and monckeberg medial calcific sclerosis: What is the difference? In *Jornal Vascular Brasileiro* (Vol. 20). Sociedade Brasileira de Angiologia e Cirurgia Vascular. https://doi.org/10.1590/1677-5449.200211

Fernandes, D. C., Araujo, T. L. S., Laurindo, F. R. M., & Tanaka, L. Y. (2018). Hemodynamic Forces in the Endothelium: From Mechanotransduction to Implications on Development of Atherosclerosis. In *Endothelium and Cardiovascular Diseases: Vascular Biology and Clinical Syndromes* (pp. 85–95). Elsevier. https://doi.org/10.1016/B978-0-12-812348-5.00007-6

Friedman, M. H., Deters ', O. J., Mark ', F. F., Bargeron ', C. B., & Hutchins, G. M. (1983). Arterial Geometry Affects Hemodynamics A Potential Risk Factor for Atherosclerosis. In *Atherosclerosis* (Vol. 46).

Gallo, D., Bijari, P. B., Morbiducci, U., Qiao, Y., Xie, Y., Etesami, M., Habets, D., Lakatta, E. G., Wasserman, B. A., & Steinman, D. A. (2018). Segment-specific associations between local haemodynamic and imaging markers of early atherosclerosis at the carotid artery: An in vivo human study. *Journal of the Royal Society Interface*, *15*(147). https://doi.org/10.1098/rsif.2018.0352

Gallo, D., Steinman, D. A., & Morbiducci, U. (2015). An Insight into the Mechanistic Role of the Common Carotid Artery on the Hemodynamics at the Carotid Bifurcation. *Annals of Biomedical Engineering*, *43*(1), 68–81. https://doi.org/10.1007/s10439-014-1119-0

Garth, C., Tricoche, X., & Scheuermann, G. (2004). Tracking of vector field singularities in unstructured 3D time-dependent datasets. *IEEE Visualization 2004 - Proceedings, VIS 2004*, 329–336. https://doi.org/10.1109/VISUAL.2004.107

Gasser, T. C. (2021). Continuum Mechanics. In *Vascular Biomechanics* (pp. 91–165). Springer, Cham. https://doi.org/10.1007/978-3-030-70966-2_3

Giddens, D. P., Zarins, C. K., & Glagov, S. (1993). *The Role of Fluid Mechanics in the Localization and Detection of Atherosclerosis*. http://biomechanical.asmedigitalcollection.asme.org/

Ku, D. N., Giddens, D. P., Zarins, C. K., & Glagov, S. (1985). *Pulsatile Flow and Atherosclerosis in the Human Carotid Bifurcation Positive Correlation between Plaque Location and Low and Oscillating Shear Stress*. http://ahajournals.org

Kunov, M. J., Steinman, D. A., & Ross Ethier, C. (1996). Particle Volumetric Residence Time Calculations in Arterial Geometries. *Journal of Biomechanical Engineering*, *118*, 158–164. http://biomechanical.asmedigitalcollection.asme.org/

Lee, S. W., Antiga, L., Spence, J. D., & Steinman, D. A. (2008). Geometry of the carotid bifurcation predicts its exposure to disturbed flow. *Stroke*, *39*(8), 2341–2347. https://doi.org/10.1161/STROKEAHA.107.510644

Liu, X., Sun, A., Fan, Y., & Deng, X. (2014). Physiological Significance of Helical Flow in the Arterial System and its Potential Clinical Applications. *Annals of Biomedical Engineering 2014 43:1*, *43*(1), 3–15. https://doi.org/10.1007/S10439-014-1097-2

Lusis, A. J. (2000). Atherosclerosis. In *Nature* (Vol. 407, Issue 6801, pp. 233–241). https://doi.org/10.1038/35025203

MacLean, N. F., & Roach, M. R. (1998). Thickness, taper, and ellipticity in the aortoiliac bifurcation of patients aged 1 day to 76 years. *Heart and Vessels 1998 13:2*, *13*(2), 95–101. https://doi.org/10.1007/BF01744592

Malota, Z., Glowacki, J., Sadowski, W., & Kostur, M. (2018). Numerical analysis of the impact of flow rate, heart rate, vessel geometry, and degree of stenosis on coronary hemodynamic indices. *BMC Cardiovascular Disorders*, *18*(1). https://doi.org/10.1186/S12872-018-0865-6

Mazzi, V., de Nisco, G., Hoogendoorn, A., Calò, K., Chiastra, C., Gallo, D., Steinman, D. A., Wentzel, J. J., & Morbiducci, U. (2021). Early Atherosclerotic Changes in Coronary Arteries are Associated with Endothelium Shear Stress Contraction/Expansion Variability. *Annals of Biomedical Engineering*, *49*(9), 2606–2621. https://doi.org/10.1007/s10439-021-02829-5

Mazzi, V., Gallo, D., Calò, K., Najafi, M., Khan, M. O., de Nisco, G., Steinman, D. A., & Morbiducci, U. (2020). A Eulerian method to analyze wall shear stress fixed points and manifolds in cardiovascular flows. *Biomechanics and Modeling in Mechanobiology*, *19*(5), 1403–1423. https://doi.org/10.1007/S10237-019-01278-3/FIGURES/16

Mazzi, V., Morbiducci, U., Calò, K., de Nisco, G., Rizzini, M. L., Torta, E., Caridi, G. C. A., Chiastra, C., & Gallo, D. (2021). Wall shear stress topological skeleton analysis in cardiovascular flows: Methods and applications. In *Mathematics* (Vol. 9, Issue 7). MDPI AG. https://doi.org/10.3390/math9070720

Meiselman, H. J., & Baskurt, O. K. (2003). Blood Rheology and Hemodynamics. *Seminars in Thrombosis and Hemostasis*, *29*(5), 435–450.

Mohamied, Y., Rowland, E. M., Bailey, E. L., Sherwin, S. J., Schwartz, M. A., & Weinberg, P. D. (2015). Change of Direction in the Biomechanics of Atherosclerosis. *Annals of Biomedical Engineering*, *43*(1), 16–25. https://doi.org/10.1007/S10439-014-1095-4/FIGURES/4

Mohamied, Y., Sherwin, S. J., & Weinberg, P. D. (2017). Understanding the fluid mechanics behind transverse wall shear stress. *Journal of Biomechanics*, *50*, 102–109. https://doi.org/10.1016/j.jbiomech.2016.11.035

Morbiducci, U., Kok, A. M., Kwak, B. R., Stone, P. H., Steinman, D. A., & Wentzel, J. J. (2016). Atherosclerosis at arterial bifurcations: Evidence for the role of haemodynamics and geometry. *Thrombosis and Haemostasis*, *115*(3), 484–492. https://doi.org/10.1160/TH15-07-0597/ID/JR0597-9

Morbiducci, U., Mazzi, V., Domanin, M., de Nisco, G., Vergara, C., Steinman, D. A., & Gallo, D. (2020). Wall Shear Stress Topological Skeleton Independently Predicts Long-Term Restenosis After Carotid Bifurcation Endarterectomy. *Annals of Biomedical Engineering*, *48*(12), 2936–2949. https://doi.org/10.1007/s10439-020-02607-9

Motomiya, M., & Karino, T. (n.d.). Flow Patterns in the Human Carotid Artery Bifurcation. In *STROKE* (Vol. 15, Issue 1). http://ahajournals.org

Papaioannou, T., & Stefanadis, C. (2005). Vascular Wall Shear Stress: Basic Principles and Methods. *Hellenic Journal of Cardiology*, *46*, 9–15.

Peiffer, V., Sherwin, S. J., & Weinberg, P. D. (2013a). Does low and oscillatory wall shear stress correlate spatially with early atherosclerosis? A systematic review. In *Cardiovascular Research* (Vol. 99, Issue 2, pp. 242–250). https://doi.org/10.1093/cvr/cvt044

Peiffer, V., Sherwin, S. J., & Weinberg, P. D. (2013b). Computation in the rabbit aorta of a new metric - the transverse wall shear stress - to quantify the multidirectional character of disturbed blood flow. *Journal of Biomechanics*, *46*(15), 2651–2658. https://doi.org/10.1016/j.jbiomech.2013.08.003

Perktold, K., Karner, G., Leuprecht, A., & Hofer, M. (1999). *Influence of non-newtonian flow behavior on local hemodynamics*.

Rapp, B. E. (2017). Fluids. *Microfluidics: Modelling, Mechanics and Mathematics*, 243–263. https://doi.org/10.1016/B978-1-4557-3141-1.50009-5

Roth, G. A., Mensah, G. A., Johnson, C. O., Addolorato, G., Ammirati, E., Baddour, L. M., Barengo, N. C., Beaton, A., Benjamin, E. J., Benziger, C. P., Bonny, A., Brauer, M., Brodmann, M., Cahill, T. J., Carapetis, J. R., Catapano, A. L., Chugh, S., Cooper, L. T., Coresh, J., … Fuster, V. (2020). Global Burden of Cardiovascular Diseases and Risk Factors, 1990-2019: Update From the GBD 2019 Study. In *Journal of the American College of Cardiology* (Vol. 76, Issue 25, pp. 2982–3021). Elsevier Inc. https://doi.org/10.1016/j.jacc.2020.11.010

Schulz, U. G. R., & Rothwell, P. M. (2001). Major variation in carotid bifurcation anatomy: A possible risk factor for plaque development? *Stroke*, *32*(11), 2522–2529. https://doi.org/10.1161/HS1101.097391/FORMAT/EPUB

Secomb, T. W. (2016). Hemodynamics. *Comprehensive Physiology*, *6*(2), 975–1003. https://doi.org/10.1002/cphy.c150038

Sousa, P. C., Pinho, F. T., Alves, M. A., & Oliveira, M. S. N. (2016). A review of hemorheology: Measuring techniques and recent advances. In *Korea Australia Rheology Journal* (Vol. 28, Issue 1, pp. 1–22). Korean Society of Rheology. https://doi.org/10.1007/s13367-016-0001-z

Steinman, D. A., Thomas, J. B., Ladak, H. M., Milner, J. S., Rutt, B. K., & David Spence, J. (2002). Reconstruction of carotid bifurcation hemodynamics and wall thickness using computational fluid dynamics and MRI. *Magnetic Resonance in Medicine*, *47*(1), 149–159. https://doi.org/10.1002/MRM.10025

Tucker, W. D., Arora, Y., & Mahajan, K. (2022). *Anatomy, Blood Vessels*.

Wasilewski, J., Kiljański, T., & Mirota, K. (n.d.). *Biomechanical Aspects of Atherosclerosis*. https://www.researchgate.net/publication/277515934

Weinberg, P. D. (2022). Haemodynamic Wall Shear Stress, Endothelial Permeability and Atherosclerosis—A Triad of Controversy. In *Frontiers in Bioengineering and Biotechnology* (Vol. 10). Frontiers Media S.A. https://doi.org/10.3389/fbioe.2022.836680

Wentzel, J. J., Chatzizisis, Y. S., Gijsen, F. J. H., Giannoglou, G. D., Feldman, C. L., & Stone, P. H. (2012). Endothelial shear stress in the evolution of coronary atherosclerotic plaque and vascular remodelling: Current understanding and remaining questions. In *Cardiovascular Research* (Vol. 96, Issue 2, pp. 234–243). https://doi.org/10.1093/cvr/cvs217

Zhou, J., & Fung, Y. C. (1997). The degree of nonlinearity and anisotropy of blood vessel elasticity. *Proceedings of the National Academy of Sciences of the United States of America*, *94*(26), 14255. https://doi.org/10.1073/PNAS.94.26.14255

Sitography

17.2D: Systemic and Pulmonary Circulation - Medicine LibreTexts. Retrieved June 16, 2022, from https://med.libretexts.org/Bookshelves/Anatomy_and_Physiology/Book%3A_Anatomy_and_Physiology_(Boundless)/17%3A_Cardiovascular_System%3A_The_Heart/17.2%3A_Circulation_and_Heart_Valves/17.2D%3A_Systemic_and_Pulmonary_Circulation

An Overview of Blood – Anatomy and Physiology. Retrieved June 16, 2022, from https://opentextbc.ca/anatomyandphysiologyopenstax/chapter/an-overview-of-blood/

Arteriosclerosis / atherosclerosis - Symptoms and causes - Mayo Clinic. (n.d.). Retrieved June 16, 2022, from https://www.mayoclinic.org/diseases-conditions/arteriosclerosis-atherosclerosis/symptoms-causes/syc-20350569

blood - Plasma | Britannica. Retrieved June 16, 2022, from https://www.britannica.com/science/blood-biochemistry/Plasma

Classification & Structure of Blood Vessels | SEER Training. Retrieved June 16, 2022, from https://training.seer.cancer.gov/anatomy/cardiovascular/blood/classification.html

Common Carotid Artery - Physiopedia. Retrieved June 17, 2022, from https://www.physiopedia.com/Common_Carotid_Artery

Structure of the Heart | SEER Training. Retrieved June 16, 2022, from https://training.seer.cancer.gov/anatomy/cardiovascular/heart/structure.html

The Vascular Modelling Toolkit. Www.Vmtk.Org. Retrieved July 8, 2022, from http://www.vmtk.org/